Research Article

3D Tumor-Engineered Model Replicating the Osteosarcoma Stem Cell Niche and *In Vivo* Tumor Complexity

Giada Bassi,* Arianna Rossi, Elisabetta Campodoni, Monica Sandri, Patrizia Sarogni, Stefania Fulle, Valerio Voliani, Silvia Panseri, and Monica Montesi*

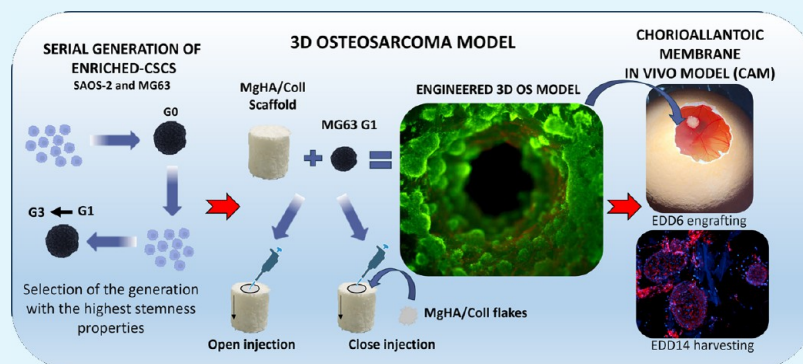Cite This: *ACS Appl. Mater. Interfaces* 2024, 16, 55011−55026

Read Online

ACCESS | 📊 Metrics & More | 📖 Article Recommendations | 🆂🅸 Supporting Information

ABSTRACT: Osteosarcoma, among all bone sarcomas, remains a challenge despite the unwavering efforts of medical professionals and scientists. To address this, the scientific community is actively pursuing the development of three-dimensional (3D) *in vitro* models to faithfully replicate the heterogeneity of osteosarcoma, thereby facilitating the reliable preclinical screening of potential therapies. In this study, we present the latest advancements in engineering an *in vitro* 3D osteosarcoma model comprising enriched Cancer Stem Cells (CSCs) and a hybrid hydroxyapatite-based scaffold (MgHA/CoII). The improvement of the model occurred through two primary steps: (1) serial passaging of sarcospheres as the CSCs enrichment system and (2) the optimization of the structural configuration of the niche in the scaffold. Two injection-mediated approaches of sarcosphere seeding were designed and extensively characterized *in vitro* and *in vivo* Chorioallantoic Membrane (CAM) models to explore their biological properties and tumorigenic potential. The combination of the selected enriched-CSCs and custom-made seeding into the scaffold resulted in the development of 3D osteosarcoma models exhibiting tumor-like features *in vitro* and tumorigenic properties *in vivo*. The outcomes of this study offer prospects for future endeavors involving more complex systems capable of replicating specific malignant tumor behaviors (metastatic process and drug resistance), pushing the discovery of new therapeutic strategies for clinical applications.

KEYWORDS: *tumour engineering, osteosarcoma, biomaterials, enriched-CSCs, CAM models*

■ INTRODUCTION

Osteosarcoma (OS) represents the most common malignant tumor among bone sarcomas, with an incidence of two-thirds of primary bone tumors.[1] It exhibits significant heterogeneity, resulting in several subtypes based on the differentiation degree, histological variation, and biological behavior.[2] Notable advances in OS treatment were made in the 1970s by incorporating adjuvant and neoadjuvant chemotherapy into therapeutic regimens, improving the 5-year survival rate of patients with localized disease from 11% to >60%.[3] However, recent progress has not shown substantial improvements, leading to a poor prognosis for metastatic patients and relapses, with an estimated 5-year survival rate of <30.[4]

A key factor contributing to OS heterogeneity is the small percentage (0.05−1%) of Cancer Stem Cells (CSCs),[5] which are pivotal in the tumorigenesis process. CSCs possess stem-like properties that enable uncontrolled amplification and alteration of molecular/cellular phenotypes, consequently fostering multidrug resistance mechanisms.[6] Moreover, CSCs exhibit dormancy, rendering them refractory to conventional therapies.[7]
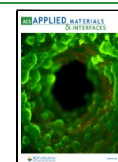
A critical aspect of OS is the tumor microenvironment's (TME) heterogeneity, called niche, which facilitates intricate crosstalk between CSCs and other constituents (e.g., extracellular matrix, tumor and nontumor cells). Specifically,

the extracellular matrix within the niche comprises three-dimensional (3D) acellular networks of macromolecules offering structural and biochemical support and regulating tumor environments (e.g., hypoxia, acid pH, low nutrients level),[8,9] cell communication, adhesion, migration, proliferation, and differentiation.[10] Cancer cells produce an osteoid matrix, propelling tumor progression and metastatic dissemination through reciprocal interactions.[11]

Traditionally, biological research and drug discovery rely on standard *in vitro* bidimensional (2D) cell culture systems, inadequately summarizing such complex diseases.[12] Sarcospheres, a more sophisticated *in vitro* enriched-CSCs model, emerged in 2005[13] when Gibbs et al. demonstrated self-renewing cell colonies forming suspended spheroids, selecting anoikis-resistant cells, a crucial hallmark of malignant behavior.[14] Additionally, the serial passage of sarcospheres has shown improvements in the undifferentiated features, sphere-forming capacity, and tumoral properties of such enriched-CSCs model in various tumors.[15−18] Despite the high potential of this *in vitro* enriched-CSCs model, serial sarcospheres need improvement due to the demonstrated limitations.[19,20] In recent years, the scientific community has pursued engineering of the dynamic tumor ecosystem, adopting a novel Tissue Engineering approach known as Tumour Engineering. This approach involves engineering *in vitro* 3D scaffold-based cell culture models, aiming to overcome these limitations by replicating in vivo TME intricacies, establishing a more predictive platform for preclinical studies.[21]

This study aims to provide a comprehensive characterization of the stem and tumor features of four serial generations of sarcospheres (Gs) derived from human osteosarcoma cell lines, implemented on a 3D bone mimetic scaffold. A hybrid composite scaffold derived from the nucleation and growth of Magnesium-doped hydroxyapatite (MgHA) on self-assembling collagen fibers (MgHA/Coll)[22] was selected for its faithful recapitulation of the bone matrix's biochemical composition and formation process.[23] Through precise cell seeding procedures and selection of the optimal Gs, advanced *in vitro* 3D scaffold-based models resembling the osteosarcoma CSCs-niche (3D OS models) were successfully developed and explored *in vitro* and *in vivo* CAM models.[24] The hypothesis underlying this study is that the development of a 3D model that combines two tissue engineering approaches (sarcospheres and the use of bone mimetic scaffolds) may better replicate the conditions of the tumor microenvironment present *in vivo*. The ultimate long-term goal is to create complex models for more predictive *in vitro* studies that is capable of enhancing and making more effective basic biology research and drug screening.

■ MATERIALS AND METHODS

Cell Culture. Human Osteosarcoma MG63 and SAOS-2 cell lines were purchased from the American Type Culture Collection (ATCC CRL-1427 and ATCC HTB-85, respectively). MG63 cells were cultured in DMEM/F-12 GlutaMAX (Gibco), 10% fetal bovine serum (FBS) (Gibco), and 1% Penicillin/Streptomycin mixture (Pen/Strep) (Gibco). The SAOS-2 cell line was cultured in McCoy's 5 Modified Medium (Gibco), supplemented with 15% FBS and 1% Pen/Strep. Cells were incubated at 37 °C under 5% CO_2 and controlled humidity conditions. Cells were detached from the flask by trypsinization and centrifuged. The cell number and viability

were assessed using the Trypan Blue Dye Exclusion Test. All cell handling procedures were performed in sterile conditions under a laminar flow hood.

Sarcosphere-Forming Culture and Serial Sarcospheres. Sarcospheres were obtained from MG63 and SAOS-2 cells using Sarcosphere-Forming Culture.[13] The cells were seeded in Ultra-Low Attachment (U.L.A.) T25 flasks (Corning) at a density of 5000 cells/cm^2 in DMEM/F12 GlutaMAX medium supplemented with a specific cocktail of factors: 10 μL/mL N2 (Gibco), 20 μL/mL B27 (Gibco), 0.1 μL/mL Recombinant Human Fibroblast Growth Factor-basic (hFGFb) (Invitrogen), and 0.01 μL/mL Recombinant Human Epidermal Growth Factor (hEGF) (PeproTech) under serum-free conditions. The cocktail was added to the cells every 2/3 days. Cell cultures were incubated for up to 10 days at 37 °C, 5% CO_2, and controlled humidity conditions. The sarcospheres of the generation 0 (G0) were thus obtained, collected, and centrifuged, and a combination of enzymatic and mechanical dissociation was performed. Single cells were counted and seeded again under Sarcosphere-Forming Culture for 10 days of induction to reform sarcospheres, namely, generation 1 (G1). Sarcospheres were serially passaged for a total of 4 G reported here as G0, G1, G2, and G3 for MG63 and SAOS-2 cells.

Sarcospheres Proliferation. The proliferation of Gs in MG63 and SAOS-2 cells was assessed by using PrestoBlue Cell Viability Reagent (Invitrogen). Single cells of each generation were seeded in the U.L.A. 96-well plates under Sarcosphere-Forming Culture with a density of 15 000 cells/cm^2. The assay was performed at 1, 3, 7, and 10 days of culture following the manufacturer's instructions. At each time point, cells were incubated with 10% (v/v) PrestoBlue Reagent for 2 h at 37 °C, 5% CO_2. Cells were collected, centrifuged, and the supernatant was analyzed using a Fluoroskan Microplate Fluorometer (Thermo Fisher Scientific) at 544 nm excitation and 590 nm emission. For each time point, a total of 6 biological replicates per sarcosphere generation were analyzed ($N = 6$).

Sarcospheres-Forming Efficiency (SFE). The SFE of MG63 and SAOS-2 Gs was assessed as reported.[25] Briefly, single cells of each generation were seeded in U.L.A. 96well plates under Sarcosphere-Forming Culture conditions with a density of 1,000 cells/well, 3,000 cells/well, and 6,000 cells/well.[13,14] At 10 days of culture, 10 fields per well were randomly acquired at 10× magnification using an Optical Microscope (Nikon). The total SFE was calculated as a percentage (%) of the total number of sarcospheres in each well divided by the cell density $[(n°\ \text{sarcospheres/cell density})*100]$. The size distribution of Gs was calculated as a percentage (%) with respect to the total number of sarcospheres, according to a defined dimensional range (50−99 μm, 100−199 μm, ≥200 μm diameter). The diameter of the sarcospheres was measured by using ImageJ Software (ImageJ 1.53t), and only sarcospheres with diameter ≥50 μm were considered. One experiment was performed and a biological triplicate was carried out at each cell density for each generation ($N = 3$).

Stem Cell Frequency (SCF). The frequency of one stem cell within MG63 Gs was assessed using the Limiting Dilution Assay (LDA).[26] Briefly, single cells of each generation were serially diluted at a density of 1000, 500, 250, 50, 10, and 1 cell/well in U.L.A. 96-well plates and incubated under Sarcosphere-Forming Culture. At 14 days of culture, the number of wells per condition containing sarcospheres was

counted using the Optical Microscope. Only sarcospheres with a diameter ≥ 50 μm were considered. The data were analyzed by Extreme Limiting Dilution Analysis (ELDA) software (https://bioinf.wehi.edu.au/software/elda/) reporting: the dose (cell density), the tested (number of cultures tested), the response (number of positive cultures, thus containing sarcospheres), and the group (population group to which cells belong, thus the generation number). The results were displayed as a scatter plot graph with the corresponding trend line of linear regression; the Y-axis reported the nonresponding log fraction , and the X-axis represented the number of seeded cells/well, and the slope of the trend line showed the log-active cell fraction. The 95% confidence interval is reported as dotted lines, and the data value with zero negative response is represented by a down-pointing triangle. Two experiments were performed, and a total of 16 biological replicates were performed for each cell density ($N = 16$).

Migration and Invasion Analysis. The migration and invasion ability of MG63 Gs was carried out by Transwell Inserts for 24-well Plate with an 8.0 μm pore size membrane (Corning). For migration, single cells of each generation were plated in the top chamber of the inset at a density of 100,000 cells/cm^2 under serum-free conditions, and 20% FBS was used in the lower chamber as a chemoattractant. For invasion, the membrane of the inset was previously coated with 100 μL/cm^2 Matrigel GFR (Growth Factor Reduced Basement Membrane Matrix, Corning) in serum-free medium for 30 min of incubation at 37 °C. After 4 days of culture, the cells that failed to migrate/invade membrane pores were removed using a wet cotton swab. The cells that colonized the lower surface of the membrane were fixed in 4% paraformaldehyde (PFA), permeabilized in 0.1% Triton-X 100, and stained with 0.5% Crystal Violet solution. A total of 6 images per membrane were randomly acquired using an Optical Microscope and the cells were counted by ImageJ Software. For each generation, two biological replicates were used for migration and invasion analysis ($N = 2$).

Synthesis of 3D MgHA/Coll Scaffolds. The scaffold was obtained by a biomineralization process, as reported by Krishnakumar et al.[22] Briefly, an acid aqueous suspension was prepared by dispersing 150 g of type I collagen gel (Typeone Biomaterials S.r.l., Calimera, LE, Italy) into phosphoric acid solution (2.41 g in 500 mL; H$_3$PO$_4$, 85 wt %, Sigma-Aldrich) at room temperature. A basic aqueous suspension was obtained by adding 0.35 g of magnesium chloride (MgCl$_2$·6H$_2$O, 99 wt %, Sigma-Aldrich) in a calcium hydroxide suspension (2.71 g in 500 mL; Ca(OH)$_2$, 95 wt %, Sigma-Aldrich) at room temperature. The acid suspension was dropped into the basic one at 25 °C under stirring conditions, causing the nucleation of MgHA nanocrystals onto the self-assembling collagen fibers, thus forming the MgHA/Coll hybrid hydrogel. After 2 h of maturation at 25 °C, the hydrogel was washed and converted into a porous material by freeze-drying (-40 °C and $+25$ °C) for 48 h under 0.086 mbar vacuum conditions (5 Pa, LIO 3000 PLT). The scaffolds were stabilized, preserving the biological cues of the collagen, by dehydrothermal (DHT) cross-linking treatment at 160 °C for 48 h under a pressure of 0.01 mbar. The scaffolds (ϕ: 9 mm; h:6 mm) were sterilized by 25 kGy γ-ray irradiation before use.

MgHA/Coll Scaffolds Morphological Analysis. The samples morphology was analyzed by Scanning Electron Microscopy (SEM). The semples were mounted onto aluminum stubs using black carbon tapes and coated with gold, using Polaron Sputter Coater E5100 (Polaron Equipment, Watford, Hertfordshire, United Kingdom). Then, they were examined using high-resolution environmental scanning electron microscopy (ESEM) (Quanta 600 FEG, FEI Company, Hills-boro, OR, United States) under a pressure of 0,1 mTorr at an accelerating voltage of 7 or 10 kV.

The total porosity of scaffolds was calculated by the density method[27] according to the formula:

total porosity (%)=100-(ρ/ρ_theoretical $\times 100$), where ρ is scaffold density determined with the following equation:

$\rho=W/(\pi \times [(D/2)]^2 \times H)$, in which W is weight, D is diameter, and H is height of the scaffold.

The theoretical density of the material is calculated from the theoretical density and weight fraction (X_A, X_B, etc.) of each reagent in the following way:

ρ_theoretical $= (\rho$_theoretical $(A) \times X\_A)+ (\rho$_theoretical $(B) \times X\_B))$. All values were expressed as the mean $\pm$ SEM ($N = 3$).

The macropore volume percentage was calculated by the water squeezing method.[28] Briefly, the scaffold was equilibrated in deionized water for 1 h, and weighed (Mswollen), then squeezed to remove the water filling pores and weighed again (Msqueezed). Macropores volume was calculated using the following equation:

Macroporosity (%)= ($M\_swollen-M\_squeezed$)/$M\_swollen \times 100$. All values were expressed as the mean $\pm$ SEM ($N = 3$).

Inductively Coupled Plasma-Optical Emission Spectrometry (ICP-OES). The quantitative determination of Mg^{2+}, Ca^{2+}, and PO$_4^{3-}$ ions that constitutes the inorganic mineral component of the MgHA/Coll Scaffolds was assessed by ICP-OES (Agilent Technologies 5100 ICP-OES, Santa Clara, USA). Briefly, 40 mg of sample was dissolved in 2 mL nitric acid (65 wt %), followed by subsequent sonication and dilution with 100 mL of milli-Q water.

Thermogravimetric Analysis (TGA). The MgHA/Coll Scaffolds were analyzed by TGA using STA 449/C Jupiter (Netzsch, Germany) on 10 mg of sample placed in an alumina crucible under airflow, brought from room temperature to 1100 °C at a heating rate of 10 °C/min.

X-Ray Diffraction (XRD). The MgHA/Coll Scaffolds' XRD patterns were recorded by a Bruker (Karlsruhe, Germany) AXS D8 Advance diffractometer in reflection mode with CuKα radiation (λ= 1,54178 Å) generated at 40 kV and 40 mA and equipped with a Lynx-eye position-sensitive detector. XRD spectra were recorded in the 2θ range from 20° to 60° with a step size (2θ) of 0.02° and a counting time of 0.5 s.

Fourier Transform Infrared Spectroscopy in the Attenuated Total Reflection Mode (FTIR-ATR). A small flake of freeze-dried MgHA/Coll Scaffold was used to perform the FTIR-ATR analysis using a Ni-colet iS5 spectrometer (Thermo Fisher Scientific Inc., Waltham, MA, USA) with a resolution of 2 cm^{-1} by accumulation of 64 scans covering the 4000 to 400 cm^{-1} range, using a diamond ATR accessory model iD7.

MgHA/Coll Scaffolds Swelling and Degradation Behavior. The samples swelling ratio (Qs) was measured by immersion in PBS 1X at pH 7.4 with 0.1% (w/v) NaN$_3$ at 37 °C. At predetermined time points, excess water was removed with a piece of absorbent paper, and the sample was weighed. The swelling ratio (Qs) was evaluated using the equation:
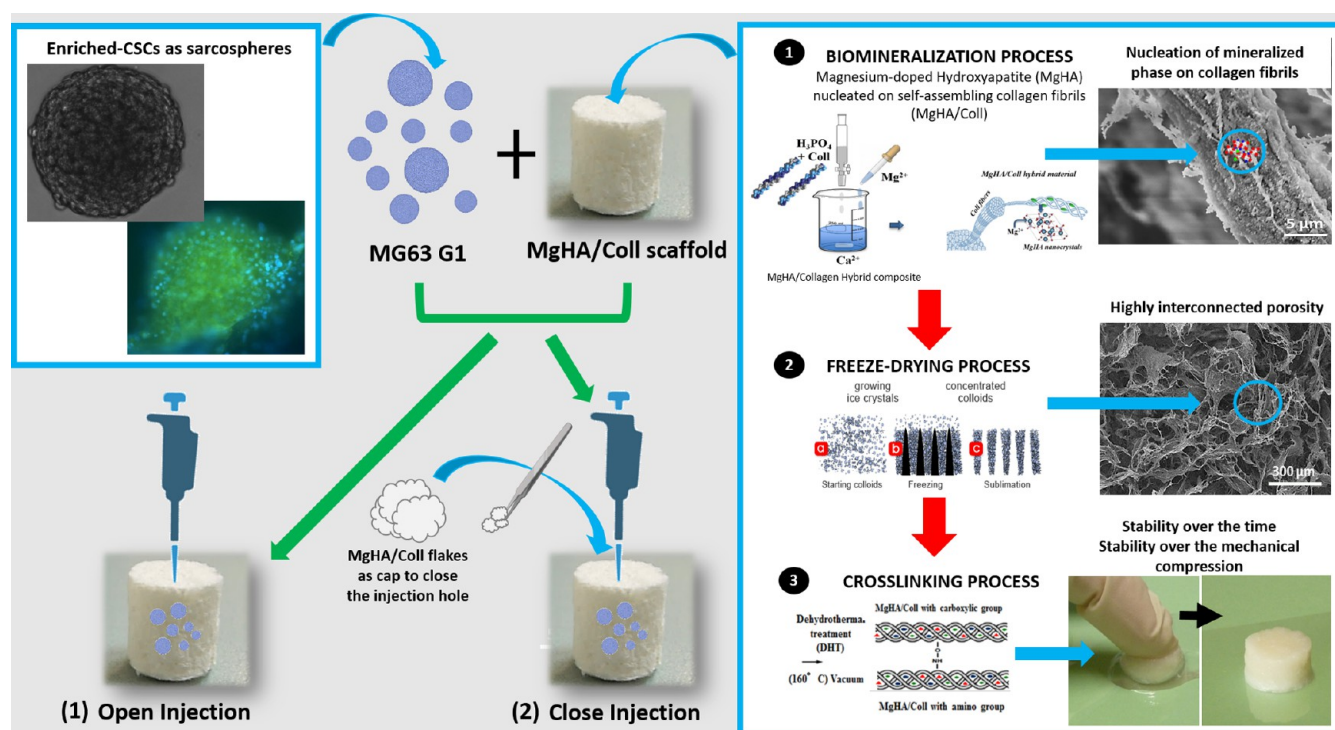
Figure 1. Schematic representation of the optimized procedure for seeding of MG63 G1 into 3D MgHA/Coll scaffolds. The combination of G1 sarcospheres of the MG63 cell line and the 3D MgHA/Coll scaffold is reported and used for the optimization of the tumor niche. The synthesis procedure of the MgHA/Coll scaffold is reported.

$Qs = (Ws - Wd)/Wd$, where Ws is the weight of the swollen sample and Wd is the initial weight of the dried sample ($N = 3$).

For the degradation test, the scaffolds were immersed in the PBS 1X at 37 °C, and at predetermined time points, they were removed from it, washed twice with milli-Q water, freeze-dried, and subsequently weighed. The Degradation Percentage (D) was evaluated using the equation:

$D(\%) = (Wi - Wf)/Wi \times 100$, where Wi is the initial weight of the dried sample and Wf is weight of the freeze-dried sample degraded at a specific time point ($N = 3$).

Optimization of MG63 G1 Seeding in the 3D MgHA/Coll Scaffold. Two different injection-mediated approaches for MG63 G1 seeding in the 3D MgHA/Coll scaffolds were designed and developed, as graphically reported in Figure 1. Briefly, the MgHA/Coll scaffold was preconditioned in serum-free media for 24 h before the seeding. The MG63 cell line was seeded at a density of 50 000 cells/well in U.L.A. 6-well plates and cultured under sarcosphere-forming culture conditions, as previously described, to obtain G1. The G1 sarcospheres of each well were separately collected, centrifuged, and seeded, by injecting 20 μL of drop/scaffold using a p200 tip. In one group of scaffolds, labeled as 'close injection,' wet flakes of MgHA/Coll material were manipulated by tweezers and used as a cap to close the scaffold hole derived from the injection of G1. In a second group of samples, labeled as 'open injection,' no caps were used (Figure 1). In both groups, after 20 min of incubation to allow sarcosphere preadhesion to the scaffold, the 3D OS models were maintained under sarcosphere-forming culture conditions for a total of 7 days at 37 °C, 5% CO$_2$, and controlled humidity. For the gene expression analysis performed to biologically characterize the 3D OS models *in*

vitro, the scaffold-free sarcospheres grown in the sarcosphere-forming conditions described above were used as a control.

A preliminary evaluation of the injection-based approach was performed after 14 days of Sarcosphere-Forming Culture ($N = 1$).

***In Vivo* Tumour Chorioallantoic Membrane (CAM) Model.** Both 3D OS models, open and close injection, were optimized in terms of dimensions ($\sim$ h: 3 mm; d: 3 mm; 1.5 mm thick) and weight ($\leq$50 mg) to be engrafted on the membrane of the chick embryo at embryonic day 6 of development (EDD6).[24] The open injection ($\sim$20 mg weight), the closed one ($\sim$40 mg weight), and the scaffold without cells as control group (CTR) ($\sim$20 mg weight) were engrafted on the CAM after 7 days of Sarcosphere-Forming Culture *in vitro*. For the grafting procedure, a small window was opened on the blunt end of the egg, and fine tweezers were used to deposit each 3D scaffold on the respective CAM. In total, six biological replicates of open injection ($N = 6$) and a duplicate of both close injection ($N = 2$) and the control ($N = 2$) were engrafted. After grafting, the eggs were placed back in an incubator (FIEM MG 140/200) set at 37.5 °C/99.5 °F and 60% humidity. Morphological changes and growth monitoring started at EDD10 until EDD14. At EDD14, the 3D scaffolds were harvested and their weights were determined. The harvested samples were fixed in 4% PFA or 4% formalin and then processed for further biological analysis.

Live and Dead Assay. The viability of MG63 G1 injected into the MgHA/Coll scaffold was preliminarily analyzed by Live and Dead Assay. Briefly, on days 3, 7, and 14 of culture, the samples were washed in PBS 1X and incubated in the Live and Dead solution composed of Acetoxymethyl Calcein (AM-calcein) 2 μM and Ethidium Homodimer-1 (EthD-1) 4 μM in PBS 1X for 15 min at 37 °C in the dark. Samples were washed

in PBS 1X and images were acquired using the Inverted Ti-E Fluorescence Microscope (Nikon) with FITC and TRITC filters for green calcein detection of live cells and red ethidium detection of dead cells. For the experiment, one biological replicate was performed ($N = 1$).

Gene Expression Analysis. The gene expression was analyzed by relative quantification in the Gs of both cell lines and in the 3D OS models. For each generation, single cells of sarcospheres were seeded in U.L.A. 6-well plates with a density of 5,000 cells/cm^2 were incubated under Sarcospheres-Forming Culture for 10 days. Then, the sarcospheres were collected, centrifuged, and suspended in Tri Reagent (Invitrogen) combined with mechanical dissociation. For 3D OS models, each scaffold was separately collected and homogenized by two passages in Tri Reagent and pestle-mediated breaking of the scaffold after 7 days of Sarcosphere-Forming Culture. RNA extraction and purification were performed using the Direct-zol RNA MiniPrep kit (Zymo Research), following the manufacturer's instructions. RNA quantification and purity degree were evaluated using the NanoDrop One Microvolume UV−vis Spectrophotometer (Thermo Fisher Scientific), following the manufacturer's instructions. Reverse Transcription of RNA into single-strand cDNA was performed using the High-Capacity cDNA Reverse Transcription Kit (Applied Biosystem) starting from 500 ng of purified RNA, following the manufacturer's instructions. Real-Time PCR with TaqMan Gene Expression Assay Kits (Applied Biosystem) was carried out. Octamer-binding transcription factor 4 (OCT-4, Hs00999632_g1), Homeobox protein NANOG (NANOG, Hs04399610_g1), and Sex determining region Y-box (SOX-2, Hs01053049_s1) were analyzed for both the Gs and the 3D OS models. Hypoxia-Inducible Factor 1 alpha (HIF-1α, Hs00153153_m1), Interleukin 6 (IL-6, Hs00174131_m1), and Notch homologue 1 translocation-associated (NOTCH-1, Hs01062014_m1) were analyzed in the 3D OS models. G0 and scaffold-free sarcospheres were used as control groups for the Gs and for the 3D OS models, respectively. Actin-β (ACTB, Hs01060665_g1) was used as a housekeeping gene. One experiment was performed, and three biological replicates for each condition were analyzed using three technical replicates ($N = 3$). Data were collected from the QuantStudio 1 Real-Time PCR System (Applied Biosystem) and the relative quantification of target genes was assessed by the Comparative Threshold (CT) method ($\Delta\Delta$CT), where relative gene expression level equals to $2^{-\Delta\Delta CT}$.[29]

Immunohistochemistry. The 3D OS models and the tumor grafts were fixed in 4% formalin, following the manufacturer's instructions. The samples were dehydrated with an increasing scale of alcohol solutions (from 70 to 100% v/v) and cleared in a xylene reagent (Sigma-Aldrich) under vacuum conditions. The samples were embedded in paraffin, and a semiautomatic rotary microtome (Histo-Line Laboratories) was used to dissect 5 μm sections. The sections were deparaffinized at 59 °C, cleared in xylene, hydrated with decreasing alcohol solution concentrations (from 100 to 70% v/v), and rinsed in water. For the 3D OS models, one biological replicate for each condition was used ($N = 1$). For the tumor grafts, two biological replicates of open injection ($N = 2$) and one biological replicate of close injection ($N = 1$) were performed. For immunohistochemistry, the UltraTek HRP (Horseradish peroxidase) Anti-Polyvalent (AEC) Staining System (Histo-Line Laboratories) was performed on the

3D OS models, following the manufacturer's instructions. For the tumor grafts, the UltraTek Alk-Phos Anti-Polyvalent (Fast Red) Staining System (Histo-Line Laboratories) was used, following the manufacturer's instructions. For both types of samples, the sections were incubated with primary antibodies for SOX-2 (1:200, MA1014, Thermo Fisher Scientific), OCT-4 (2 μg/mL, MA1104, Life Technologies), and NANOG (1:50, MA1017, Thermo Fisher Scientific) following the manufacturer's instructions. For the 3D OS models, primary antibodies for HIF-1α (1:800, 36169S, Cell Signaling Technology) and NOTCH-1 (1:200, 4380S, Cell Signaling Technology) were also used, following the manufacturer's instructions. Primary antibodies for CD133 (Prominin-1, 1:25, MA1219, Invitrogen), Ki67 (1:100, MA541135, Invitrogen), PECAM-1 (Platelet and endothelial cell adhesion molecule 1 or cluster of differentiation 31 − CD31, 1:100, 89C2, Cell Signaling), and vWF (Von Willebrand Factor, 1 μg/mL, ab201336, Abcam) were performed on tumor grafts, following the manufacturer's instructions. Nuclear Fast Red (Sigma-Aldrich) and Methyl Green (Sigma-Aldrich) were used as counterstaining in the 3D OS models and tumor grafts, respectively, for cell nuclei identification, following the manufacturer's instructions. The sections were dehydrated in increasing scale of alcohol solutions, cleared in xylene, and mounted by histology mount. Images were acquired using an Optical Microscope.

Histological Staining. The 3D OS models and the tumor grafts embedded in paraffin as previously reported were used. The obtained sections were deparaffinized and hydrated as previously reported. For both types of samples, haematoxylin (Fluka, Sigma-Aldrich) and eosin (Histo-Line Laboratories) (H&E staining was performed, following the manufacturer's instructions. For the tumor grafts, Von Kossa (Sigma-Aldrich) and Alizarin Red (Sigma-Aldrich) staining was also performed, following the manufacturer's instructions, and Nuclear Fast Red was used as counterstaining for cell nuclei identification. The sections were dehydrated and mounted using a histology mount, and images were acquired using an Optical Microscope.

Actin and DAPI Staining. The morphology of MG63 G1, the 3D OS models, and the tumor grafts was analyzed by Actin and DAPI staining. Briefly, the MG63 G1 and the tumor grafts were fixed in 4% PFA, following the manufacturer's instructions. Then, the samples were embedded in an OCT (Optimal Cutting Temperature Compound, Histo-Line Laboratories) and cryosectioned in 5 μm sections by a cryostat (Histo-Line Laboratories). The 3D OS models previously embedded in paraffin were used, and the obtained sections were deparaffinized and hydrated as previously reported. The sections were permeabilized in 0.1% Triton-X 100 in PBS 1X and stained with Rhodamine Phalloidin Actin red 555 ready probes (Invitrogen) for F-actin filament detection. DAPI staining was used as counterstaining for cell nuclei identification. The sections were mounted using Fluor Save reagent, and images were acquired using an Inverted Ti-E Fluorescence Microscope with TRITC and DAPI filters. For MG63 G1, one biological replicate was performed ($N = 1$). For tumor grafts, one biological replicate for open injection and CTR was performed ($N = 1$).

Statistical Analysis. Statistical analysis was performed using GraphPad Prism Software (8.0.1 version). The results of PrestoBlue Cell Viability Reagent are reported in the graph as mean normalization with respect to day 1 $\pm$ SEM and were
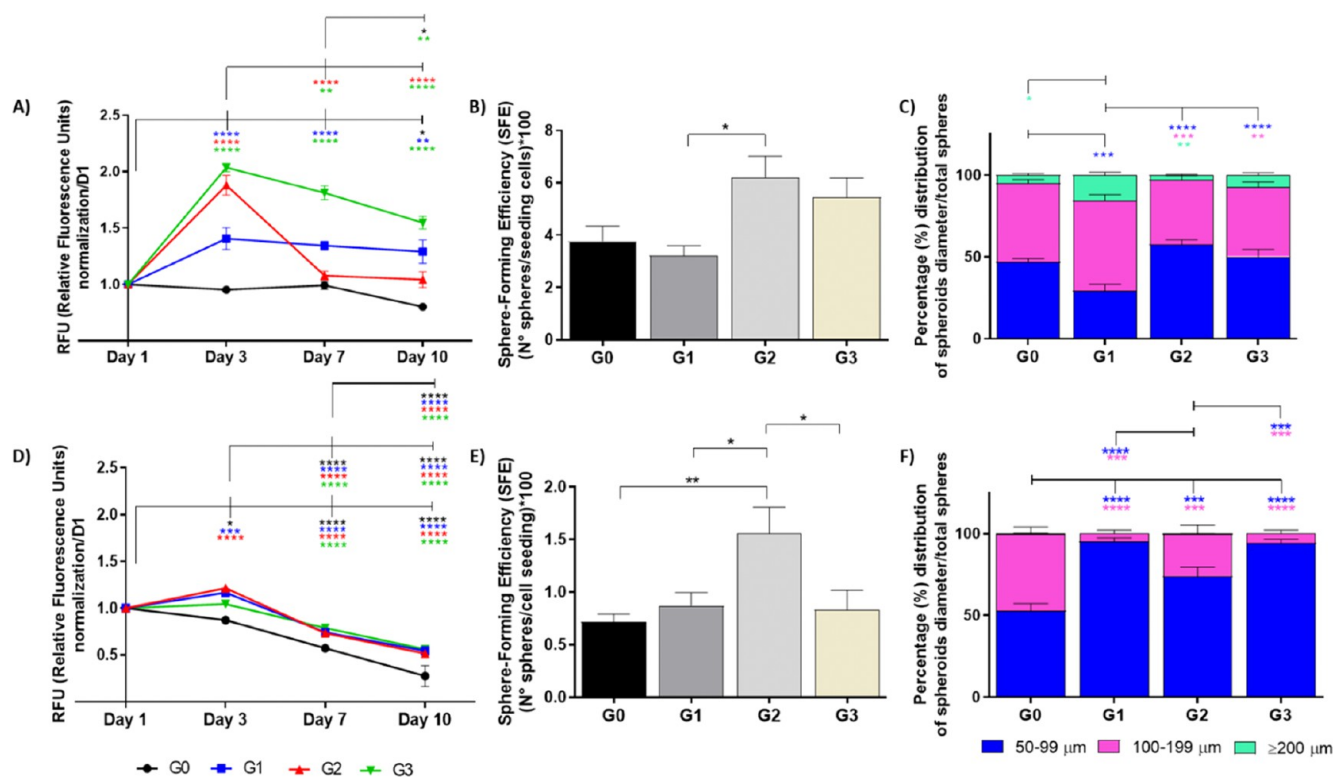
Figure 2. Proliferation, SFE, and size distribution of MG63 and SAOS-2 Gs. Presto Blue Cell Viability Reagent for MG63 Gs (A) and SAOS-2 Gs (D) as mean ± SEM. Statistical analysis over the time was performed by two-way ANOVA and Tukey's multiple comparisons test, and it is reported for each generation ($N = 6$); the SFE for MG63 Gs (B) and SAOS-2 Gs (E) is reported in the graphs as total % SFE, and statistical analysis was performed by one-way ANOVA and Tukey's multiple comparisons test ($N = 3$); the size distribution of MG63 Gs (C) and SAOS-2 Gs (F) is reported as % distribution of spheroids diameter/total spheres, and the data were analyzed by two-way ANOVA and Tukey's and Sidak's multiple comparisons tests ($N = 3$). * p value ≤ 0.05, ** p value ≤ 0.01, *** p value ≤ 0.001, **** p value ≤ 0.0001.

analyzed by two-way analysis of variance (two-way ANOVA) and Tukey's multiple comparisons test.

The SFE values are reported in the graphs as mean SFE values ± SEM, while the size distribution is expressed as percentage (%) distribution of spheroids diameter/total spheres ± SEM; statistical analysis was performed by two-way ANOVA and Tukey's and Sidak's multiple comparisons tests.

Stem Cell Frequency was performed on LDA by ELDA software[26] assuming the Poisson Distribution. The results were analyzed by the Pairwise test for differences between coupled generations and by the Chi-Square test as an overall test for differences between any of the generations.

The results of migration and invasion evaluation are reported in the graphs are mean of counted cells ± SEM and were analyzed by one-way analysis of variance (one-way ANOVA) and Tukey's multiple comparisons test.

The results of qRT-PCR are reported in the graphs as fold-change expression relative to the experimental control ± SEM and were analyzed by two-Way ANOVA and Tukey's multiple comparisons test.

RESULTS

Stem and Tumor Properties of MG63 and SAOS-2 Gs.
The sarcosphere generations, reported as G0, G1, G2, and G3, were analyzed in terms of cell proliferation and Sarcospheres-Forming Efficiency (SFE) up to 10 days of culture, showing significant differences in cell behaviors (Figure 2). MG63 Gs showed a peak of cell proliferation after 3 days of culture

(Figure 2A), with a statistically significant difference of G1, G2, and G3 compared to day 1. G1, G2, and G3 showed higher proliferative potential compared to G0, while G2 and G3 were highly proliferative compared to G1 (Figure S1A). Starting from day 7, a statistically significant decrease in cell growth was reported in all of the Gs tested, except for MG63 G1, which displayed the most stable proliferation trend (Figure 2A). Indeed, after an increase on day 3, MG63 G1 proliferation reached a plateau with live cells significantly higher than those of G0 and G2 up to day 10 (Figure S1A). A similar proliferation trend was observed for SAOS-2 Gs (Figure 2D). Indeed, on day 3, a significant cell proliferation in G1 and G2 compared to day 1 was observed. However, despite the significantly higher live cell number in G1, G2, and G3 compared to G0 up to 10 days (Figure S1B), the proliferative capacity in all the Gs statistically significantly decreases over time (Figure 2D).

The SFE and size distribution analysis were performed according to a defined dimensional range (50−99 μm, 100−199 μm, ≥ 200 μm diameter) (Figure 2B,C,E and F). Higher SFE values, diameter size, and a well-preserved round-shape spheroidal phenotype were reported with MG63 Gs compared to SAOS-2 (Figures 2, S2). A marked increase of SFE was shown in G2 of both cell lines; MG63 reported a SFE value of 6.20% ± 0.81 in G2 compared to 3.77% ± 0.58, 3.22% ± 0.38, and 5.45% ± 0.74 of G0, G1, and G3, respectively, with a statistically significant difference between G2 and G1 (Figure 2B). SAOS-2 Gs showed the same SFE trend, reporting a significant increase in G2 with respect to G0, G1, and G3;
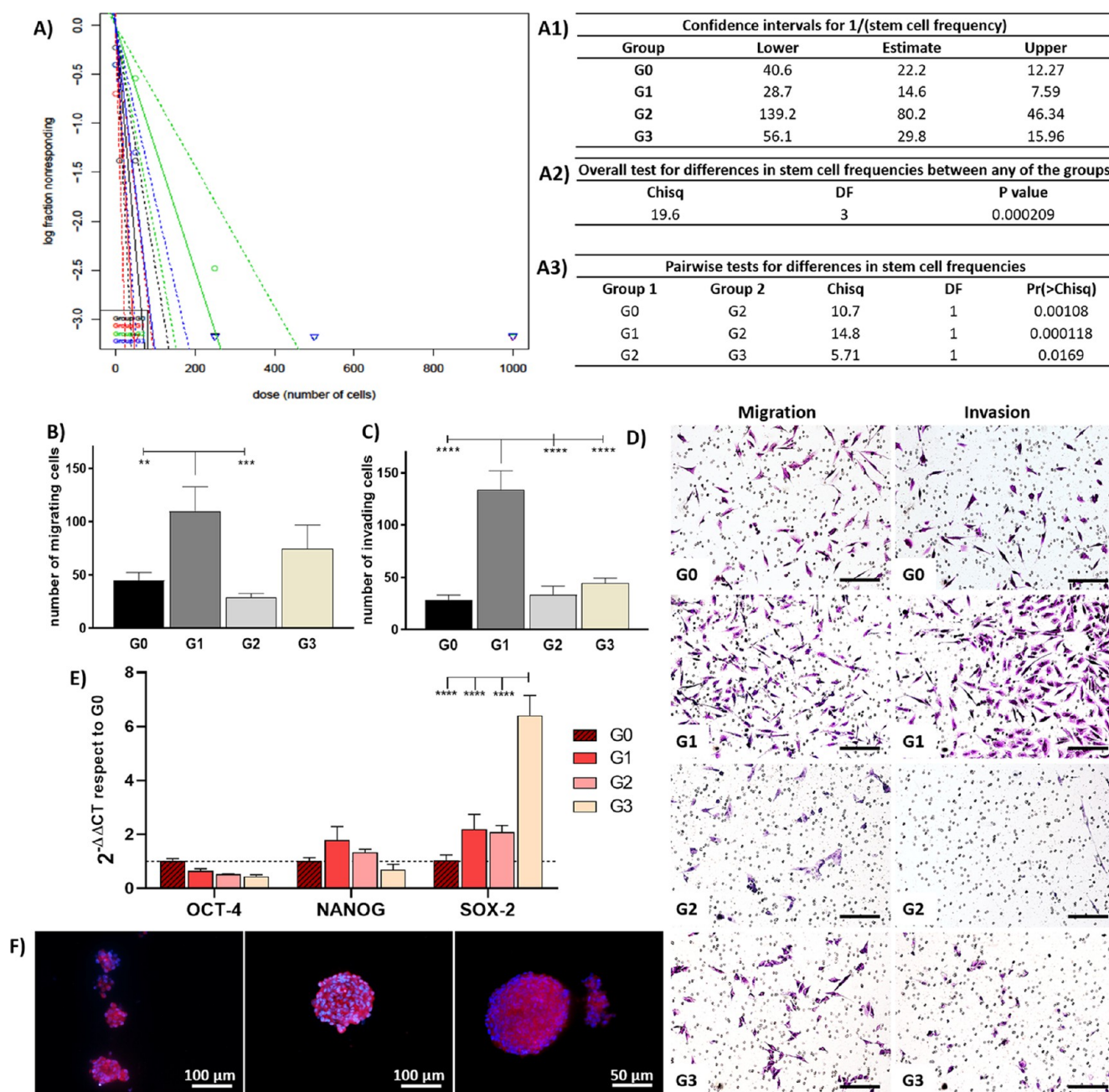
Figure 3. SCF, Migration and Invasion ability, gene expression, and cell morphology of MG63 Gs. (A, A1, A2, A3) SCF ($N = 16$): (A) scatter plot graph with the corresponding trend line of linear regression with 95% confidence interval in dotted lines and data value with zero negative response in down-pointed triangle; (A1) frequency intervals for 1 stem cell by Poisson distribution; (A2) overall significant differences between any of the generations by Chi-square test; (A3) statistically significant differences between coupled generations by Pairwise test. (B) Cell migration and (C) invasion as the mean of counted cells ± SEM. Statistically significant differences among generations are reported. Data were analyzed by one-way ANOVA and Tukey's multiple comparison test ($N = 2$). (D) Crystal violet staining of migrating and invasive cells. Scale bars 200 μm. (E) qRT-PCR of stem markers as fold-change expression relative to G0 ± SEM. Data were analyzed by two-way ANOVA and Tukey's multiple comparison test ($N = 3$). (F) Actin and DAPI stainings of G1. F-actin filaments are colored red, and cell nuclei blue ($N = 1$). ** p value ≤ 0.01, *** p value ≤ 0.001, **** p value ≤ 0.0001.

specifically, a SFE value of 1.56% ± 0.24 was shown by G2 compared to 0.71% ± 0.07, 0.87% ± 0.12, and 0.83% ± 0.18 of G0, G1, and G3, respectively (Figure 2E).

Despite these results, the size distribution showed a different tendency in both cell lines (Figure 2C, F). MG63 G1 showed a significantly different distribution compared to other Gs; the 55.18% ± 3.62 of MG63 G1 reached a 100−199 μm diameter range, statistically different with respect to G2 and G3 (Figure 2C), and to the only 29.28% ± 4.02 of G1 with diameters

ranging in 50−99 μm (Figure S3A). The majority of MG63 G0 showed a 100−199 μm diameter range (48.19% ± 2.23), while G2 and G3 were able to form sarcospheres with a lower diameter ranging in 50−99 μm (57.70% ± 2.74 and 50.01% ± 4.47 for G2 and G3), with a statistically significant difference compared to G1. In addition, MG63 G1 was able to form a high number of sarcospheres with a diameter ≥200 μm, with a significant 15.53% ± 1.97 with respect to 4.98% ± 1.12 and 2.85% ± 0.61 of G0 and G2 (Figure 2C).
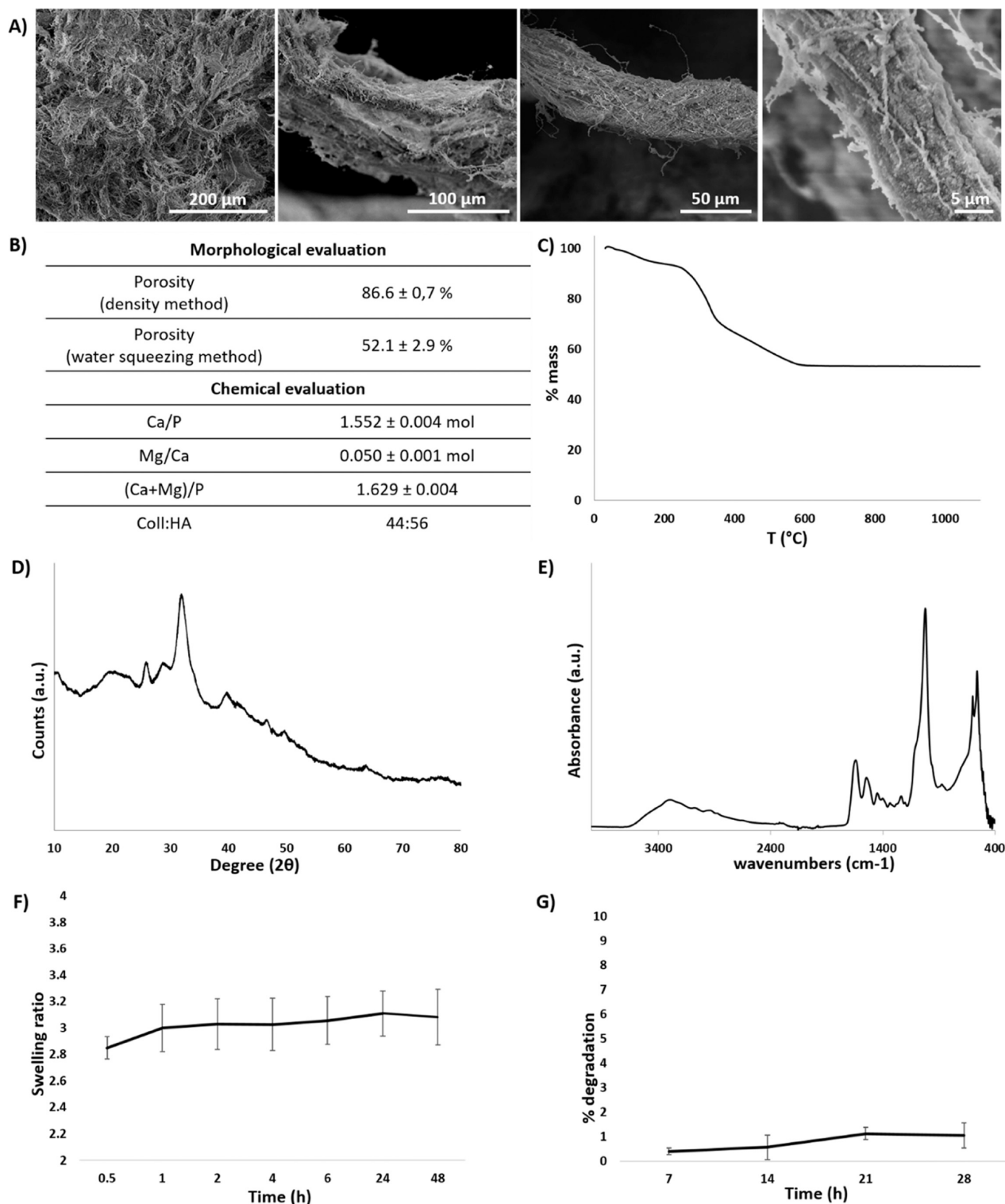
Figure 4. Characterization of the 3D MgHA/Coll scaffolds. (A) SEM images ($N = 3$). (B) Dimensional properties (total and macroporosity) and chemical composition by ICP-EOS ($N = 8$). (C) Thermal decomposition profile by TGA: the weight loss in % of mass is used to determine the organic/inorganic ratio ($N = 8$). (D) XRD pattern: peaks at 26° and 32° indicate the 002 and 211 reflect€s ($N = 8$). (E) FTIR profile ($N = 8$). (F) Time-dependent swelling behavior: time after soaking in PBS 1X on X-axis ($N = 8$). (G) Degradation profile after 7, 14, 21, and 28 days in PBS 1X ($N = 8$).

Differently, the diameter of SAOS-2 sarcospheres was lower compared to that of MG63, with a higher % in the range of 50−99 μm in all Gs (Figure 2F).

The Stem Cell Frequency (SCF), migration, invasiveness, gene expression, and cell morphology were investigated in MG63 Gs (Figure 3). The SCF as frequency of 1 stem cell plotted with 95% confidence interval was found to be highly variable among Gs (Figure 3A, A1). G1 estimated the lowest confidence interval with a frequency of 1 stem cell every 14.6 cells (1:14.6), compared to 1:22.2, 1:80.2, and 1:29.8 for G0,
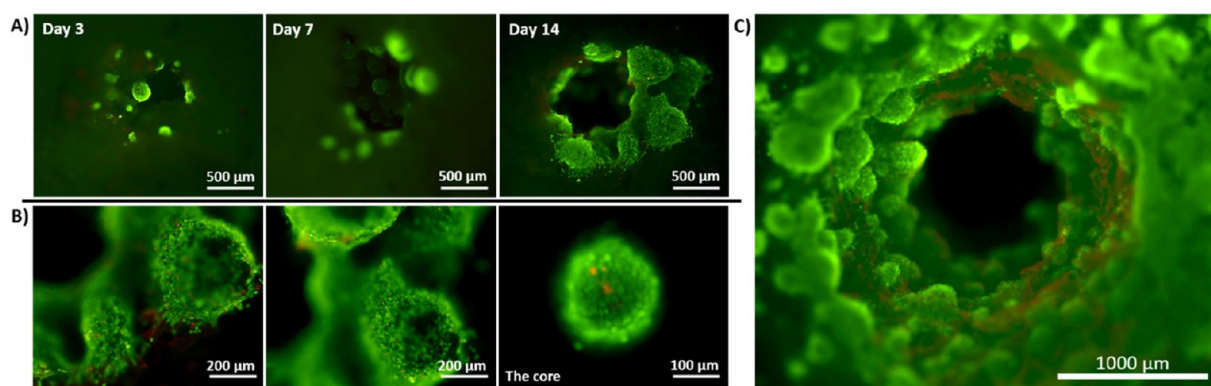
Figure 5. Preliminary evaluation of cell viability in the 3D injection-based cell culture. (A) Growth of MG63 G1 inside the injection hole for upto day 14. (B) Spheroidal phenotype of G1 at 14 days of culture with few dead cells in the core. (C) Representative image of G1 colonization of the injection hole ($N = 1$). Live cells are colored green and dead cells in red.

G2, and G3 (Figure 3A1), reporting significant difference with respect to G2. The statistical analysis reported a significant frequency in G0 and G3 compared to G2 (Figure 3A3). The test for differences in stem cell frequency between any generations reported a statistically significant Chi-Square as an overall discrepancy in SCF (Figure 3A2).

The migration and invasion analysis confirmed G1 as the generation with the highest migratory and invasive potential (Figure 3B−D). G1 reported a significantly higher number of migrating cells with respect to G0 and G2 (Figure 3B,D), and the same behavior was observed in terms of the number of invading cells, as G1 showed an enhanced invasive potential with respect to G0, G2, and G3 (Figure 3C,D).

The gene expression profile of stem markers reported a pronounced upregulation in G1 for SOX-2 (~2.18 fold-change) and also for NANOG (~1.79 fold-change), even without significant difference compared to the other Gs. A significantly higher expression of SOX-2 was observed in G3 (~6.40 fold-change), while both OCT-4 and NANOG did not show significant changes compared to G0 (Figure 3E). The G1 morphology showed a preserved spheroidal phenotype with healthy cell nuclei and actin filaments (Figure 3F).

Characterization of the 3D MgHA/Coll Scaffolds as Bone-Like Matrices. The SEM was used to investigate the three-dimensional structure of the sample (Figure 4). An isotropic structure with randomly distributed and interconnected macro- and microporosity is shown. The total porosity was assessed to be above 80% and was controlled by the amount of water present in the hydrogel during the freeze-drying process (Figure 4B). At higher magnification, the self-assembled collagen mineralized fibers that clearly showed the presence of the MgHA nanoparticles fully embedded and homogeneously distributed on the collagen fiber matrix were appreciated as a typical feature of the biomineralization process (Figure 4A).

The ICP-OES indicated that the hybrid scaffold MgHA/Coll contains a Mg/Ca ratio of 0.05 and (Mg+Ca)/P molar ratio of 1.63, compared to the typical Ca/P = 1.67 of stoichiometric apatites, indicating the presence of substituted and poorly crystalline phases (Figure 4B).

The TGA as assessment of the mineral phase content in the MgHA/Coll scaffold reported a 44:56 ratio of Coll to MgHA (Figure 4C). The TGA curve displayed three primary weight loss stages. The first stage occurred between 25 and 160 °C and was attributed to the release of adsorbed and bonded water. The second stage occurred between 160 and 360 °C and was due to the degradation of Type I collagen. The final stage, which occurred between 360 and 660 °C, was due to the complete combustion of organic residues. The residual weights corresponded to the mineral phase content (Figure 4C).

The XRD profile exhibited broad diffraction peaks, indicating a hydroxyapatite phase with low crystallinity and nanometric sizes, as an indicator of a pure hydroxyapatite phase and the absence of secondary phases (Figure 4D).

The FTIR spectra of the Coll/MgHA scaffold (Figure 4E) reported typical peaks of amide (I, II, III) stretching and bending vibrations at 1640, 1545, and 1236 cm^{-1}, respectively, corresponding to the α-helical structure. A shoulder at 1713 cm^{-1} was reported to be representative of the ester bonds induced by dehydrothermal treatment.[22] The chemical interaction between the mineral phase MgHA and collagen fibers is confirmed by the shift from 1340 to 1337 cm^{-1}, which is due to the chemical bond between the carboxylic groups of collagen and the Ca^{2+} ions of the apatite. The spectrum revealed peaks of the phosphate ion PO$_4^{3-}$ (474, 569, 602, 962, 1045, and 1091 cm^{-1}) and OH− (633 and 3572 cm^{-1}) groups as typical hydroxyapatite peaks. The bands at 3497 and 1638 cm^{-1} indicated the presence of a lattice water in the material (Figure 4E).

The cross-linking stability and water fluid uptake ability were analyzed by degradation and swelling behavior under physiological conditions (37 °C and PBS 1X) (Figure 4F,G). The hydrophilic behavior of the scaffold with a water uptake of approximately three times its weight was reported (Figure 4F). A low degradability with less than 2 wt % degradation in 28 days was reported (Figure 4G), indicating the successful improvement of the scaffold stability by the DHT cross-linking process.

Optimization of the *In Vitro* 3D OS Models: Open Injection versus Close Injection. MG63 G1 sarcospheres were selected to implement the 3D OS models by injecting (20 μL of cell suspension/scaffolds) in the core of the MgHA/Coll scaffold (Figure 1). Live and Dead assays preliminarily showed that the sarcospheres were able to grow and colonize the injection hole, preserving their localization and spheroidal phenotype for upto 14 days of culture, showing a high number of live cells (Figure 5A−C).

Two different seeding conditions were investigated: close injection and open injection. In the close injection group, wet flakes of MgHA/Coll material were used as a cap to close the
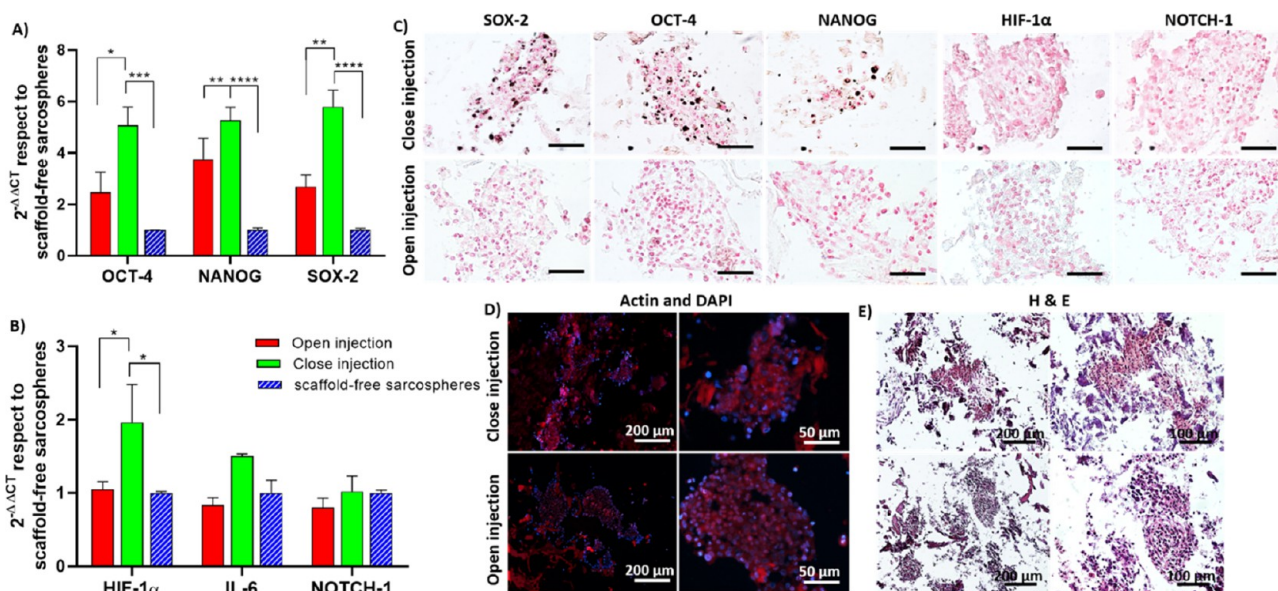
Figure 6. 3D OS models. qRT-PCR of stemness (A) and CSCs niche markers (B) as fold-change expression relative to scaffold-free G1. The graphs show the mean ± SEM. Data were analyzed by two-way ANOVA and Tukey's multiple comparisons test (N = 3). (C) Immunohistochemistry evaluation of stem and CSCs niche markers. Positivity in brown, cell nuclei in pink. Scale bars 50 μm (N = 1). (D) Actin and DAPI staining with F-actin in red and cell nuclei in blue (N = 1). (E) Hematoxylin and Eosin staining with cytoplasm in pink and cell nuclei in violet (N = 1). *p value ≤0.05, ** p value ≤0.01, *** p value ≤0.001, **** p value ≤0.0001.
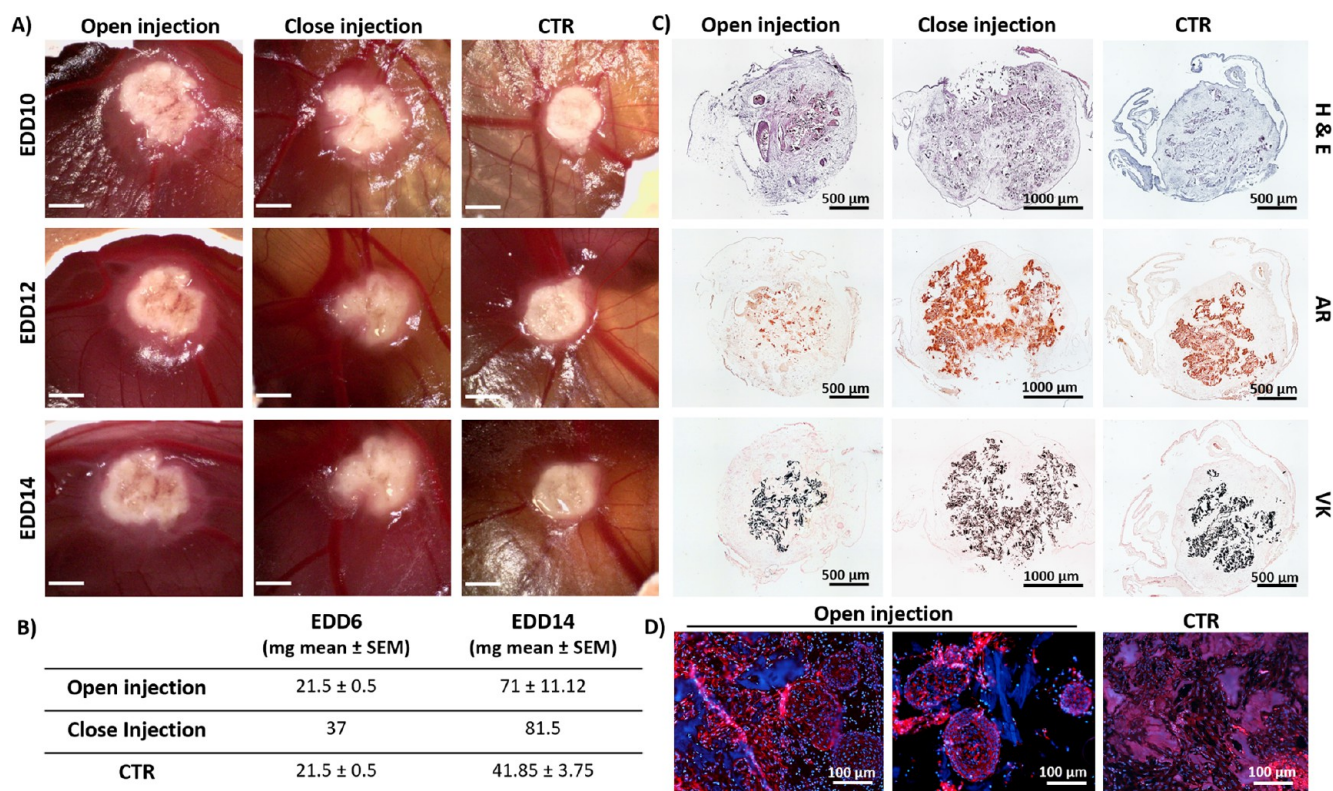

Figure 7. Growth, weight, and histological analysis of tumor grafts. (A) Growth observation of 3D OS grafted models during the experimental window. Scale bar: 2 mm. (B) Table of the weight mean in mg ± SEM; no SEM is reported for close injection as one replicate was analyzed. (C) Haematoxylin and Eosin (pink cytoplasm, violet cell nuclei), Alizarin Red (red calcium deposits), and Von Kossa (black calcium salts, pink cell nuclei) histological staining in the harvested 3D OS models. (D) Actin and DAPI staining of harvested 3D OS models; cell nuclei in blue, F actin filaments in red.

G1 injection-derived scaffold hole, while no caps were used for the open injection one.

Both groups of 3D OS models were analyzed after 7 days under sarcosphere-forming culture conditions.

The gene expression reported the upregulation of stem markers (OCT-4, NANOG, SOX-2) in both 3D OS models compared to scaffold-free G1 as a control (Figure 6A). Specifically, a significant increase in the expression of the OCT-4 (∼5.068 fold-change), NANOG (∼5.263 fold-change), and SOX-2 (∼5.798 fold-change) was reported in the close injection group, while only NANOG showed statistically significant modulation (∼3.753 fold-change) in the open injection compared to the control (Figure 6A). The close injection also showed a statistically significantly higher expression of the expression of OCT-4 and SOX-2 compared to the open injection (Figure 6A). This upregulation trend was confirmed by immunohistochemistry analysis, which reports a clear positivity of all stem markers in the close injection (Figure 6C).

In the close injection, the expression of the HIF-1α was significantly higher with respect to the control (∼1.961 fold-change) and compared to the open injection (Figure 6B).

Although not statistically significant, an upregulation trend was also observed for IL-6 (∼1.504 fold-change) in the close injection group (Figure 6B).

No relevant differences in the protein expression of the niche-related markers in both 3D OS models were observed with the immunolocalization assay (Figure 6C).

Morphological evaluation of 3D OS models did not show differences between open and closed injection (Figure 6D,E); the sarcospheres in the core of the scaffold and surrounded by the matrix preserved their spheroidal phenotype with healthy cell nuclei and actin filaments in both groups (Figure 6D,E).

In Vivo Tumour Chorioallantoic Membrane (CAM) Model Grafts: Proof of Concept. The potential tumorigenic properties of both 3D OS models were assessed on the chorioallantoic membranes (CAMs) models, a highly vascularized *in vivo* system that enables the formation of solid tumors. The models were engrafted on a small vein of the membrane of chicken embryos at the sixth Embryo Day Development (EDD6). The viability of the embryos was monitored until EDD14, where both the close and open injection groups showed a 50% survival rate with respect to the control (100%).

To allow proper adhesion of the 3D OS models to the vessels, their observation and monitoring started at EDD10 (4 days postgrafting) until EDD14 (Figure 7A).

The results indicated that both 3D OS models grew toward the interior of the membrane and their superficial measurements reached a greater volume compared to the scaffold without sarcospheres used as control (CTR). Moreover, the weights of both the open and close injection groups increased approximately 3.4- and 2.2-fold at EDD14 compared to their starting weights (Figure 7B).

The morphological analyses of the harvested 3D OS models showed clearly visible sarcospheres with a preserved spheroidal phenotype for the open injection group compared to the close injection group, in which the cells seem to be more embedded/internalized in the system (Figure 7C,D).

The Alizarin Red and Von Kossa staining did not show relevant differences in terms of calcium deposits and salts between the CTR and the 3D OS models (Figure 7C); however, the close injection reached a more extensive mineralization, which is homogeneously spread close to the membrane of the capsule, compared to the open injection and the CTR (Figure 7C).

The immunohistochemistry of stem markers showed positivity for OCT-4 and SOX-2 in the sarcospheres of both 3D OS models compared to the CTR. No positivity for NANOG was observed. A significant positivity for CD133, Ki67, and PECAM-1 was detected in both 3D OS models together with a slight positivity of vWF in the open injection compared to the CTR (Figure 8).
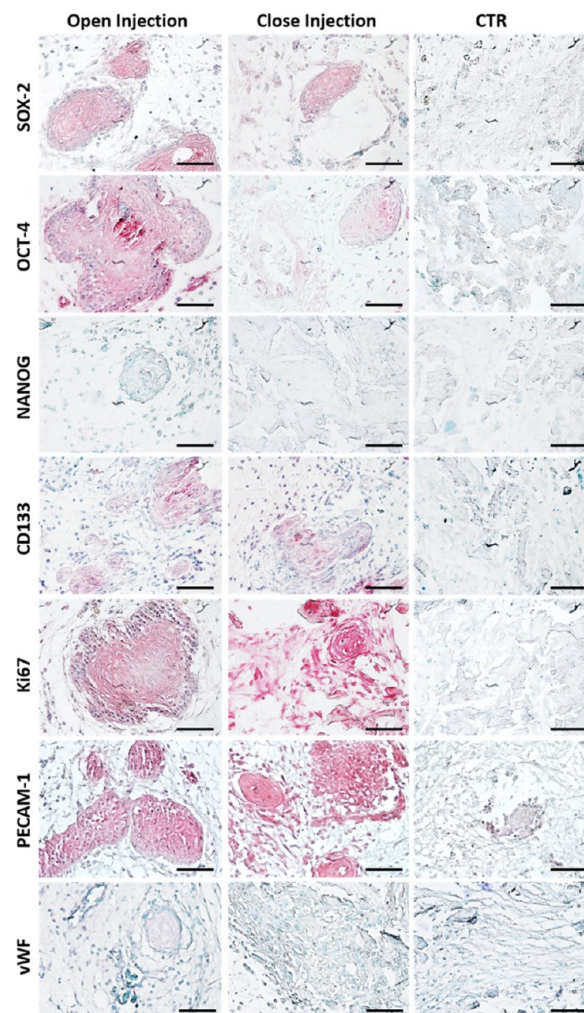

Figure 8. Immunohistochemistry analysis of the harvested 3D OS models. Immunolocalization of SOX-2, OCT-4, NANOG, CD133, Ki67, PECAM-1, and vWF in the harvested 3D OS models. Positivity in pink; cell nuclei in light blue. Scale bars: 50 μm.

■ DISCUSSION

Osteosarcoma, a highly malignant tumor, remains fatal for one-third of drug-resistant patients, it lacks effective alternative therapies. This challenge is exacerbated by a limited understanding of the disease complex biology.[30] The Cancer Stem Cells (CSCs) subset within the OS mass contributes to increasing the disease heterogeneity and instability by interacting with the tumor niche.[14]

Despite scientific efforts, replicating such complexity *in vitro* and designing predictive platforms for biological exploration and new therapeutic screening remains challenging.

To overcome these challenges and create more predictive *in vitro* systems that accurately mimic tumor complexity, especially focusing on the CSCs niche, this study combines

two established 3D engineering approaches: cellular spheroids and bone mimetic scaffolds. The 3D OS models developed here better induce CSC-specific features like stemness, spheroidal morphology, and behavior, compared to models using spheroids or cellular aggregates alone, which fail to replicate extracellular matrix complexity.[31,32]

The advantage of using naturally inspired biomaterials helps to overcome some limitations of other matrices typically proposed for the same purpose. These biomaterials offer cell-friendly porosity with appropriate interconnection and size, facilitating cellular colonization. They also ensure full biocompatibility, thus avoiding the challenges associated with preparing decellularized matrices or the cellular behavior impairment induced by synthetic materials.[33,34]

In a previous work, we proposed and successfully developed *in vitro* 3D scaffold-based models of osteosarcoma CSCs by combining bone-like hydroxyapatite (HA)-based scaffolds (i.e., a Magnesium-doped HA and collagen scaffold—MgHA/Coll—and a ceramic scaffold—HA) with sarcospheres as an enriched-CSCs model. This approach demonstrated the upregulation of specific genes associated with stemness maintenance under 3D conditions.[35]

The Sphere-Forming Culture in which CSCs, the cellular model used in this work, are enriched, has been recommended as an extremely effective method to isolate *in vitro* CSC from tumor cell lines and solid tumors.[36] Indeed, it has been demonstrated that among osteosarcoma cell lines, MG63 and SAOS-2 cells maintained in serum-deprived nonadhesive culture conditions are able to grow as spheres, to reform spheres after each dissociation passage, and then preserve the spheroidal phenotype exhibiting cancer stem cell features.[13,37] Moreover, serially reaggregated spheres have played a pivotal role in cancer research simulating growth regulation similar to solid tumors.[20] Different cell lines form spheres with distinctive morphological and functional features based on the sphere-forming method, but OS cells have not been explored in this sense.[38] However, the *in vitro* standard use of enriched-CSC shows several limitations, particularly the absence of interaction with the microenvironment, which can be overcome by employing bioengineering patterned substrates mimicking the *in vivo* TME.[19,39]

In this study, we report the *in vitro* biological characterization of serial sarcospheres and the optimization of their niche structural configuration inside the MgHA/Coll scaffold using custom-designed approaches.

Our results revealed that MG63 cells retained their spheroidal phenotype during serial passaging, as reported for other cell types,[40,41] a crucial marker indicative of self-renewing cells as one of the pillar properties of stem-like cells within tumor tissues.[42] However, SAOS-2 cells, despite the reformation of spheres after each dissociation passage, exhibited an irregular and unstable morphology, suggesting a potential loss of stem-like cells in this cell type.[43]

Additionally, MG63 Gs demonstrated a correlation between proliferation and passage number, gradually increasing proliferation across serial passages, confirming the literature.[40,44] Nonetheless, a progressively decreasing proliferation trend was observed for upto 10 days in both cell lines, potentially due to the formation of a necrotic core within sarcospheres, as seen in the typical layered structure of tumor spheroids.[40] Studies have reported that the size of the necrotic core enhances over time, while the number of proliferating cells decreases, confirming the collapsing proliferation trend of

our results.[40,45] This trend was notably pronounced in SAOS-2 cells, displaying minimal proliferation on day 3 across all Gs. Conversely, MG63 G1 maintained stable proliferation, indicating preserved proliferative capacity and stability between the necrotic core and surrounding live cells for up to 10 days.

The largest size distribution of MG63 G1 confirmed the active cell behavior and stable proliferation trend,[46] and these elements may imply a greater number of self-renewing cells within sarcospheres, as suggested by Martins-Neves et al.[47] We also found a potential directly proportional correlation between the proliferation grade and the SFE as an efficient indicator of the presence of a cell subpopulation able to form a sphere.[25] Since this property is only attributed to stem-like cells, the SFE is a universally applicable tool to assess the presence of CSCs without the use of specific markers.[48,49] However, the SFE was markedly different between the two cell lines. MG63 cells formed 3−4 times more sarcospheres per seeded cell than SAOS-2 cells, suggesting varied capabilities among osteosarcoma cell lines in forming sarcospheres due to intratumoral complexity.[50]

Given the instability of SAOS-2, MG63 Gs were chosen for detailed evaluation, serving as the enriched-CSCs model for implementing the CSC niche within the 3D MgHA/Coll scaffold. MG63 G1 estimated the lowest frequency interval for the presence of a single stem cell by LDA,[26] indicating a higher number of self-renewing cells and stable proliferation trends, making it the preferred model among Gs.[47] Moreover, MG63 G1 demonstrated the greatest migrative and invasive potential and expressed a high level of the stem markers SOX-2, OCT-4, and NANOG; these three transcription factors are able to maintain the self-renewal and pluripotency ability of CSCs, and their combined overexpression has been used to identify these critical populations in several cancers.[51−53] Overall, the biological characterization of Gs allowed the clear identification of MG63 G1 as the selected model of enriched-CSCs for the implementation of the CSCs niche in the 3D MgHA/Coll scaffold.

It is well-known that CSCs require environmental and cellular signals to survive and preserve their characteristics.[54] The microenvironment necessary for cell growth during *in vitro* studies is a determinant of the final biological behavior and the results reliability.[55] Considering the increasingly relevant challenge for mimicking the TME from the chemical, physical, biochemical, and architectural point of view, different approaches for enriched-CSCs seeding in the scaffold were proposed. In a previous study, a standard seeding of sarcospheres concerning the dripping of the cellular suspension on the material's surface was performed,[35] and different 3D OS models have been reported exploiting this simple and shallow cell seeding approach;[56,57] however, CSCs *in vivo* live in a distinct and closed anatomical niche of the tumor mass in contact with well-defined environmental conditions (i.e., hypoxia, low pH) in all directions.[54] More recent technologies (e.g., bioprinting) allow the cell incorporation into a matrix, but the bioink selection requires precise features, making them less suitable for this specific application.[58] Various studies have employed natural (i.e., collagen, silk fibroin, etc.) or synthetic materials (i.e., polyethylene glycol, polylacticcoglycolic acid, etc.) as matrix for solid tumor cells[56,59] but most models have not utilized bone-inspired materials, a critical factor in the OS in which bone composition profoundly affects tumor onset.[60] Considering this, here the synthesis, characterization, and use

of a hybrid scaffold, MgHA/Coll, resembling the biochemical composition and formation process of the bone was reported.[61]

The MgHA/Coll scaffold, which is a well-established[22] and used bone-like matrix for regenerative medicine applications,[35] was synthesized through a neutralization reaction between a basic suspension of calcium hydroxide added with magnesium chloride and an acid suspension of phosphoric acid with type I collagen. This pH variation, from 10 to 6, drove the precipitation of mineral phase nanocrystals (MgHA) and the self-assembly of collagen fibers. Simultaneously, these two processes enabled the reproduction of the bone formation process and the creation of a hybrid biomaterial that replicates the chemical features of the natural bone matrix.[62] Moreover, the low crystallinity of apatite, resulting from the biomineralization process, the low synthesis temperature, and the chemical interaction between MgHA particles and collagen molecules, indicated the achievement of a highly biomimetic mineral phase closely resembling natural bone.[22]

The material was freeze-dried to achieve a porous interconnected structure that allows cell colonization.[63]

An injection approach of MG63 G1 was proposed with the aim to confine the sarcospheres as enriched-CSCs in a biomimetic niche inside the MgHA/Coll scaffold to mimic the in vivo conditions as much as possible. Specifically, two injection-based approaches, open and close injection, for the seeding of MG63 G1 into the scaffold were proposed to overcome the limitations of the standard seeding and create a cellular niche inside a nanostructured HA-based material.[22]

It is possible to assert that the cellular and molecular responses observed in both the 3D OS models clearly demonstrated the preservation of specific CSC features. G1 overexpression of both mRNA and protein levels of transcription factors SOX-2, OCT 4, and NANOG, responsible for the maintenance of the stem phenotype,[18,64] is strictly related to the preservation of the spheroidal phenotype and proliferative profile observed.

The upregulation of IL-6 and HIF 1α in close injection highlights the role of the microenvironment in triggering CSCs phenotype[65] and inducing hypoxic conditions, which are crucial for stem feature induction in cancer cells.[66−68] HIF 1α, highly induced in hypoxic conditions, stimulate stem features regulating CSCs generation, maintenance, and survival,[69] while the pleiotropic cytokine IL-6 maintains stem properties.[70] Moreover, IL-6-mediated upregulation of HIF-1α further enhances CSCs stemness.[65] THe absence of NOTCH-1 deregulation in 3D OS models may be attributed to its dual role in tumorigenesis, depending on tissue type, genetic alterations, and receptor−ligand interactions.[65]

Moreover, the scaffold nanostructure and composition demonstrated cell-instructive performance, confirming its mimesis with the bone.[22,35] Most importantly, it is possible to assert that in the 3D OS model, the cell's confinement in a defined region of the matrix allows more recapitulation of CSCs in vivo conditions.

The in vivo pilot study performed in CAM models[71] demonstrated the tumorigenic properties of both 3D OS models. As one of the most attractive and ethical in vivo models,[72] the CAM models were used for the engrafting of 3D scaffold-based tumors, which were successfully implanted on the vascularized membrane. Tumor growth, the presence of a spheroidal phenotype and the increased mineralization of the tumor grafts represented significant marks of tumor develop-

ment potential.[73] Moreover, the expression of stem markers SOX-2, OCT-4, and CD133,[64,74] the cell proliferation regulator and marker of tumor diagnosis Ki67,[75] and PECAM-1 confirmed the successful development of the tumor in the in vivo CAM model.

Tumor neovascularization involves the formation of new blood vessels, which are crucial for tumor progression,[76,77] PECAM-1, the gene encoded for CD 31 transmembrane glycoprotein, serves as an early marker for tumor-induced angiogenesis, indicating processes like angiogenesis and vascular permeability.[78] Its positivity in both 3D OS models confirms early stage angiogenesis compared to CTR. Hypoxia, indicated by HIF-1α and IL-6 upregulation showed in our models, may contribute to CSC-mediated production of angiogenic factors and vasculogenic mimicry.[77] Moreover, vWF, a large glycoprotein highly expressed in the advanced tumor stage, was minimally observedin open injection, suggesting immature neovascularization.[79,80]

The use of 3D OS models can lead to important advancements in oncological research, and the outcomes of this study open brilliant perspectives for future implementation of more complex systems (i.e., co-culture, matrix-functionalization) able to mimic specific malignant behaviors (metastatic process, drug resistance, etc.), increasing the knowledge of tumor biology and pushing the discovery of new therapeutic strategies for clinical applications.

■ CONCLUSIONS AND OUTLOOK

Recent years have witnessed significant advancements in the field of 3D tumor engineering, achieved through the application of biomimetic strategies. These strategies aim to recreate elements of the original microenvironment, thus restoring both the form and function of the tumor mass. The proposed 3D OS models represent an innovative approach for replicating cancer behaviors. Consequently, it is reasonable to extend these strategies to comprehend tumor biology, address fundamental questions and foster ongoing interdisciplinary collaboration to unravel the complexities of cancers.

Future endeavors will concentrate on the implementation of the biochemical properties of the diseased matrix and the heterogeneity of the tumor cell population as two main pillars of the osteosarcoma, focusing on specific malignant behaviors.

■ ASSOCIATED CONTENT

ⓢ **Supporting Information**

The Supporting Information is available free of charge at https://pubs.acs.org/doi/10.1021/acsami.4c02567.

> Statistically significant differences among Gs at each time point in the proliferation by PrestoBlue Cell Viability Assay (Figure S1); representative panel of the spheroidal phenotype of Gs (Figure S2); statistically significant differences among size dimensional ranges in each Gs (Figure S3) (PDF)

■ AUTHOR INFORMATION

Corresponding Authors

Giada Bassi − *Institute of Science, Technology and Sustainability for Ceramics, National Research Council of Italy, Faenza, Ravenna (RA) 48018, Italy; Department of Neuroscience, Imaging and Clinical Science, University of Studies "G. D'Annunzio", Chieti, Chieti (CH) 66100, Italy;*

ⓘ orcid.org/0000-0001-8496-5077; Email: giada.bassi@issmc.cnr.it

Monica Montesi − *Institute of Science, Technology and Sustainability for Ceramics, National Research Council of Italy, Faenza, Ravenna (RA) 48018, Italy;* ⓘ orcid.org/0000-0002-9192-8554; Email: monica.montesi@issmc.cnr.it

Authors

Arianna Rossi − *Institute of Science, Technology and Sustainability for Ceramics, National Research Council of Italy, Faenza, Ravenna (RA) 48018, Italy; Departmentof Chemical, Biological, Pharmaceutical and Environmental Sciences, University of Studies of Messina, Messina, Messina (ME) 98166, Italy;* ⓘ orcid.org/0000-0001-9863-7701

Elisabetta Campodoni − *Institute of Science, Technology and Sustainability for Ceramics, National Research Council of Italy, Faenza, Ravenna (RA) 48018, Italy*

Monica Sandri − *Institute of Science, Technology and Sustainability for Ceramics, National Research Council of Italy, Faenza, Ravenna (RA) 48018, Italy*

Patrizia Sarogni − *Center for Nanotechnology Innovation@ NEST, Istituto Italiano Di Tecnologia, Pisa, Pisa (PI) 56127, Italy*

Stefania Fulle − *Department of Neuroscience, Imaging and Clinical Science, University of Studies "G. D'Annunzio", Chieti, Chieti (CH) 66100, Italy*

Valerio Voliani − *Center for Nanotechnology Innovation@ NEST, Istituto Italiano Di Tecnologia, Pisa, Pisa (PI) 56127, Italy; Department of Pharmacy, School of Medical and Pharmaceutical Sciences, University of Genoa, Genoa, Genoa (GE) 16148, Italy*

Silvia Panseri − *Institute of Science, Technology and Sustainability for Ceramics, National Research Council of Italy, Faenza, Ravenna (RA) 48018, Italy*

Complete contact information is available at:
https://pubs.acs.org/10.1021/acsami.4c02567

Author Contributions

The manuscript was written through contributions of all authors. All authors have given approval to the final version of the manuscript. M.M. and G.B. conceived and designed the experiments. G.B. conducted the biological experiments. M.M., G.B., A.R., and S.P. analyzed the results. E.C. and M.S. designed synthesized and characterized the biomaterial. P.S. and V.V. provide and performed the CAM model. G.B. and M.M. wrote the paper.

Notes

The authors declare no competing financial interest.

■ ABBREVIATIONS

3D	three-dimensional
CSCs	cancer stem cells
MgHA/Coll	magnesium doped-hydroxyapatite and collagen fibers scaffold
CAM	chorioallantoic membrane model
OS	osteosarcoma
TME	tumour microenvironment
2D	bidimensional
Gs	serial generations of sarcospheres
ATCC	American Types Culture Collection
FBS	fetal bovine serum
Pen/Strep	Penicillin and Streptomycin
U.L.A.	ultra-low attachment
hFGFb	Recombinant Human Fibroblast Growth Factor-basic
hEGF	Recombinant Human Epidermal Growth Factor
SFE	sarcosphere-forming efficiency
SCF	stem cell frequency
ELDA	extreme limiting dilution analysis
Matrigel GFR	Growth Factor Reduced Basement Membrane Matrix
PFA	paraformaldehyde
DHT	dehydrothermal
EDD	embryonic day of development
PBS	phosphate-buffered saline
AM-Calcein	acetoxymethyl calcein
EthD-1	ethidium homodimer-1
OCT-4	octamer-binding transcription factor 4
NANOG	homeobox protein NANOG
SOX-2	sex determining region Y-box
HIF-1α	Hypoxia-Inducible Factor 1 alpha
IL-6	interleukin 6
NOTCH-1	Notch homologue 1 translocation-associated
ACTB	actin-β
CT	comparative threshold
H&E	haematoxylin and eosin
OCT	optimal cutting temperature compound
DAPI	4′,6-diamidino-2-phenylindole
SEM	standard error of the mean

■ REFERENCES

(1) Ferguson, J. L.; Turner, S. P. Bone Cancer: Diagnosis and Treatment Principles. *Am. Fam. Physician* **2018**, *98* (4), 205−213.

(2) Klein, M. J.; Siegal, G. P. Osteosarcoma: Anatomic and histologic variants. *Am. J. Clin. Pathol.* **2006**, *125* (4), 555−581.

(3) Pilavaki, P.; Gahanbani Ardakani, A.; Gikas, P.; Constantinidou, A. Osteosarcoma: Current Concepts and Evolutions in Management Principles. *J. Clin. Med.* **2023**, *12* (8), 2785.

(4) Spraker-Perlman, H. L.; Barkauskas, D. A.; Krailo, M. D.; Meyers, P. A.; Schwartz, C. L.; Doski, J.; Gorlick, R.; Janeway, K. A.; Isakoff, M. S. Factors influencing survival after recurrence in osteosarcoma: A report from the Children's Oncology Group. *Pediatr. Blood Cancer* **2019**, *66* (1), No. e27444.

(5) Heymann, M. F.; Lézot, F.; Heymann, D. The contribution of immune infiltrates and the local microenvironment in the pathogenesis of osteosarcoma. *Cell. Immunol.* **2019**, *343*, 103711.

(6) Moitra, K.; Lou, H.; Dean, M. Multidrug efflux pumps and cancer stem cells: Insights into multidrug resistance and therapeutic development. *Clin. Pharmacol. Ther.* **2011**, *89* (4), 491−502.

(7) Moore, N.; Lyle, S. Quiescent, slow-cycling stem cell populations in cancer: A review of the evidence and discussion of significance. *J. Oncol.* **2011**, *2011*, 396076.

(8) Flavahan, W. A.; Wu, Q.; Hitomi, M.; Rahim, N.; Kim, Y.; Sloan, A. E.; Weil, R. J.; Nakano, I.; Sarkaria, J. N.; Stringer, B. W.; et al.et al

Brain tumor initiating cells adapt to restricted nutrition through preferential glucose uptake. *Nat. Neurosci.* 2013, 16 (10), 1373−1382.

(9) Ayla, S.; Karahüseyinogluc, S. Cancer Stem Cells, Their Microenvironment and Anoikis. *Crit. Rev. Oncog.* 2019, 24 (1), 27−34.

(10) Theocharis, A. D.; Skandalis, S. S.; Gialeli, C.; Karamanos, N. K. Extracellular matrix structure. *Adv. Drug Delivery Rev.* 2016, 97, 4−27.

(11) Levental, K. R.; Yu, H.; Kass, L.; Lakins, J. N.; Egeblad, M.; Erler, J. T.; Fong, S. F.; Csiszar, K.; Giaccia, A.; Weninger, W.; et al.et al Matrix crosslinking forces tumor progression by enhancing integrin signaling. *Cell* 2009, 139 (5), 891−906.

(12) Horvath, P.; Aulner, N.; Bickle, M.; Davies, A. M.; Nery, E. D.; Ebner, D.; Montoya, M. C.; Östling, P.; Pietiäinen, V.; Price, L. S.; et al.et al Screening out irrelevant cell-based models of disease. *Nat. Rev. Drug Discovery* 2016, 15 (11), 751−769.

(13) Gibbs, C. P.; Kukekov, V. G.; Reith, J. D.; Tchigrinova, O.; Suslov, O. N.; Scott, E. W.; Ghivizzani, S. C.; Ignatova, T. N.; Steindler, D. A. Stem-like cells in bone sarcomas: Implications for tumorigenesis. *Neoplasia* 2005, 7 (11), 967−976.

(14) Brown, H. K.; Tellez-Gabriel, M.; Heymann, D. *Cancer Stem Cells In Osteosarcoma. Cancer Lett.* 2017, 386, 189−195.

(15) Hardin, H.; Yu, X. M.; Harrison, A. D.; Larrain, C.; Zhang, R.; Chen, J.; Chen, H.; Lloyd, R. V. Generation of Novel Thyroid Cancer Stem-Like Cell Clones: Effects of Resveratrol and Valproic Acid. *Am. J. Pathol.* 2016, 186 (6), 1662−1673.

(16) Pease, J. C.; Brewer, M.; Tirnauer, J. S. Spontaneous spheroid budding from monolayers: A potential contribution to ovarian cancer dissemination. *Biol. Open* 2012, 1 (7), 622−628.

(17) Cariati, M.; Naderi, A.; Brown, J. P.; Smalley, M. J.; Pinder, S. E.; Caldas, C.; Purushotham, A. D. Alpha-6 integrin is necessary for the tumourigenicity of a stem cell-like subpopulation within the MCF7 breast cancer cell line. *Int. J. Cancer* 2008, 122 (2), 298−304.

(18) Gheytanchi, E.; Naseri, M.; Karimi-Busheri, F.; Atyabi, F.; Mirsharif, E. S.; Bozorgmehr, M.; Ghods, R.; Madjd, Z. Morphological and molecular characteristics of spheroid formation in HT-29 and Caco-2 colorectal cancer cell lines. *Cancer Cell Int.* 2021, 21 (1), 204.

(19) Pastrana, E.; Silva-Vargas, V.; Doetsch, F. Eyes wide open: A critical review of sphere-formation as an assay for stem cells. *Cell Stem Cell* 2011, 8 (5), 486−498.

(20) Layer, P. G.; Robitzki, A.; Rothermel, A.; Willbold, E. Of layers and spheres: the reaggregate approach in tissue engineering. *Trends Neurosci.* 2002, 25 (3), 131−134.

(21) Cui, J.; Dean, D.; Hornicek, F. J.; Chen, Z.; Duan, Z. The role of extracelluar matrix in osteosarcoma progression and metastasis. *J. Exp. Clin. Cancer Res.* 2020, 39 (1), 178.

(22) Krishnakumar, G. S.; Gostynska, N.; Dapporto, M.; Campodoni, E.; Montesi, M.; Panseri, S.; Tampieri, A.; Kon, E.; Marcacci, M.; Sprio, S.; et al.et al Evaluation of different crosslinking agents on hybrid biomimetic collagen-hydroxyapatite composites for regenerative medicine. *Int. J. Biol. Macromol.* 2018, 106, 739−748.

(23) Fong, E. L.; Harrington, D. A.; Farach-Carson, M. C.; Yu, H. Heralding a new paradigm in 3D tumor modeling. *Biomaterials* 2016, 108, 197−213.

(24) Sarogni, P.; Mapanao, A. K.; Marchetti, S.; Kusmic, C.; Voliani, V. A Standard Protocol for the Production and Bioevaluation of Ethical In Vivo Models of HPV-Negative Head and Neck Squamous Cell Carcinoma. *ACS Pharmacol. Transl. Sci.* 2021, 4 (3), 1227−1234.

(25) Bahmad, H. F.; Cheaito, K.; Chalhoub, R. M.; Hadadeh, O.; Monzer, A.; Ballout, F.; El-Hajj, A.; Mukherji, D.; Liu, Y. N.; Daoud, G.; et al.etal Sphere-Formation Assay: Three-Dimensional in vitro Culturing of Prostate Cancer Stem/Progenitor Sphere-Forming Cells. *Front. Oncol.* 2018, 8, 347.

(26) Hu, Y.; Smyth, G. K. ELDA: Extreme limiting dilution analysis for comparing depleted and enriched populations in stem cell and other assays. *J. Immunol. Methods* 2009, 347 (1−2), 70−78.

(27) Mao, J. S.; Zhao, L. G.; Yin, Y. J.; Yao, K. D. Structure and properties of bilayer chitosan-gelatin scaffolds. *Biomaterials* 2003, 24 (6), 1067−1074.

(28) Arora, A.; Kothari, A.; Katti, D. S. Pore orientation mediated control of mechanical behavior of scaffolds and its application in cartilage-mimetic scaffold design. *J. Mech. Behav. Biomed. Mater.* 2015, 51, 169−183.

(29) Livak, K. J.; Schmittgen, T. D. Analysis of Relative Gene Expression Data Using Real-Time Quantitative PCR and the 2−ΔΔCT Method. *Methods* 2001, 25 (4), 402−408.

(30) Mohseny, A. B.; Machado, I.; Cai, Y.; Schaefer, K. L.; Serra, M.; Hogendoorn, P. C.; Llombart-Bosch, A.; Cleton-Jansen, A. M. Functional characterization of osteosarcoma cell lines provides representative models to study the human disease. *Lab. Invest.* 2011, 91 (8), 1195−1205.

(31) Bassi, G.; Grimaudo, M. A.; Panseri, S.; Montesi, M. Advanced Multi-Dimensional Cellular Models as Emerging Reality to Reproduce In Vitro the Human Body Complexity. *Int. J. Mol. Sci.* 2021, 22, 1195.

(32) Han, S. J.; Kwon, S.; Kim, K. S. Challenges of applying multicellular tumor spheroids in preclinical phase. *Cancer Cell Int.* 2021, 21 (1), 152.

(33) Chakraborty, J.; Roy, S.; Ghosh, S. Regulation of decellularized matrix mediated immune response. *Biomater. Sci.* 2020, 8 (5), 1194−1215.

(34) Park, J. H.; Jo, S. B.; Lee, J. H.; Lee, H. H.; Knowles, J. C.; Kim, H. W. Materials and extracellular matrix rigidity highlighted in tissue damages and diseases: Implication for biomaterials design and therapeutic targets. *Bioact. Mater.* 2023, 20, 381−403.

(35) Bassi, G.; Panseri, S.; Dozio, S. M.; Sandri, M.; Campodoni, E.; Dapporto, M.; Sprio, S.; Tampieri, A.; Montesi, M. Scaffold-based 3D cellular models mimicking the heterogeneity of osteosarcoma stem cell niche. *Sci. Rep.* 2020, 10 (1), 22294.

(36) Zhong, Y.; Guan, K.; Guo, S.; Zhou, C.; Wang, D.; Ma, W.; Zhang, Y.; Li, C.; Zhang, S. Spheres derived from the human SK-RC-42 renal cell carcinoma cell line are enriched in cancer stem cells. *Cancer Lett.* 2010, 299 (2), 150−160.

(37) Lim, C.; Roh, Y. H.; Yoo, S. J.; Jeong, D. K.; Nam, K. W. Identification of Stem Cell Related Gene Expression from the Osteosarcoma Cell Core Side. *J. Cancer Prev.* 2022, 27 (2), 122−128.

(38) Bissell, M. J.; Kenny, P. A.; Radisky, D. C. Microenvironmental Regulators Of Tissue Structure And Function Also Regulate Tumor Induction And Progression: The Role Of Extracellular Matrix And Its Degrading Enzymes. *Cold Spring Harbor Symp. Quant. Biol.* 2005, 70, 343−356.

(39) Rodrigues, T.; Kundu, B.; Silva-Correia, J.; Kundu, S. C.; Oliveira, J. M.; Reis, R. L.; Correlo, V. M. Emerging tumor spheroids technologies for 3D in vitro cancer modeling. *Pharmacol. Ther.* 2018, 184, 201−211.

(40) Ward Rashidi, M. R.; Mehta, P.; Bregenzer, M.; Raghavan, S.; Fleck, E. M.; Horst, E. N.; Harissa, Z.; Ravikumar, V.; Brady, S.; Bild, A.; et al.et al Engineered 3D Model of Cancer Stem Cell Enrichment and Chemoresistance. *Neoplasia* 2019, 21 (8), 822−836.

(41) Condello, S.; Morgan, C. A.; Nagdas, S.; Cao, L.; Turek, J.; Hurley, T. D.; Matei, D. β-Catenin-regulated ALDH1A1 is a target in ovarian cancer spheroids. *Oncogene* 2015, 34 (18), 2297−2308.

(42) Li, C.; Heidt, D. G.; Dalerba, P.; Burant, C. F.; Zhang, L.; Adsay, V.; Wicha, M.; Clarke, M. F.; Simeone, D. M. Identification of pancreatic cancer stem cells. *Cancer Res.* 2007, 67 (3), 1030−1037.

(43) Wang, L.; Park, P.; Lin, C.-Y. Characterization of stem cell attributes in human osteosarcoma cell lines. *Cancer Biol. Ther.* 2009, 8 (6), 543−552.

(44) Yue, D.; Zhang, Z.; Li, J.; Chen, X.; Ping, Y.; Liu, S.; Shi, X.; Li, L.; Wang, L.; Huang, L.; et al.et al Transforming growth factor-beta1 promotes the migration and invasion of sphere-forming stem-like cell subpopulations in esophageal cancer. *Exp. Cell Res.* 2015, 336 (1), 141−149.

(45) Däster, S.; Amatruda, N.; Calabrese, D.; Ivanek, R.; Turrini, E.; Droeser, R. A.; Zajac, P.; Fimognari, C.; Spagnoli, G. C.; Iezzi, G.; et al.et al Induction of hypoxia and necrosis in multicellular tumor spheroids is associated with resistance to chemotherapy treatment. *Oncotarget* 2017, 8 (1), 1725−1736.

(46) Rainusso, N.; Man, T. K.; Lau, C. C.; Hicks, J.; Shen, J. J.; Yu, A.; Wang, L. L.; Rosen, J. M. Identification and gene expression profiling of tumor-initiating cells isolated from human osteosarcoma cell lines in an orthotopic mouse model. *Cancer Biol. Ther.* **2011**, *12* (4), 278−287.

(47) Martins-Neves, S. R.; Lopes, Á. O.; Do Carmo, A.; Paiva, A. A.; Simões, P. C.; Abrunhosa, A. J.; Gomes, C. M. F. Therapeutic implications of an enriched cancer stem-like cell population in a human osteosarcoma cell line. *BMC Cancer* **2012**, *12* (1), 139.

(48) Clarke, M. F.; Dick, J. E.; Dirks, P. B.; Eaves, C. J.; Jamieson, C. H.; Jones, D. L.; Visvader, J.; Weissman, I. L.; Wahl, G. M. Cancer stem cells–perspectives on current status and future directions: AACR Workshop on cancer stem cells. *Cancer Res.* **2006**, *66* (19), 9339−9344.

(49) Jordan, C. T. Cancer stem cell biology: From leukemia to solid tumors. *Curr. Opin. Cell Biol.* **2004**, *16* (6), 708−712.

(50) Gillette, J. M.; Gibbs, C. P.; Nielsen-Preiss, S. M. Establishment and characterization of OS 99−1, a cell line derived from a highly aggressive primary human osteosarcoma. *Vitro Cell. Dev. Biol.* **2008**, *44* (3−4), 87−95.

(51) Li, X.; Wang, J.; Xu, Z.; Ahmad, A.; Li, E.; Wang, Y.; Qin, S.; Wang, Q. Expression of Sox2 and Oct4 and their clinical significance in human non-small-cell lung cancer. *Int. J. Mol. Sci.* **2012**, *13* (6), 7663−7675.

(52) Habu, N.; Imanishi, Y.; Kameyama, K.; Shimoda, M.; Tokumaru, Y.; Sakamoto, K.; Fujii, R.; Shigetomi, S.; Otsuka, K.; Sato, Y.; et al.et al Expression of Oct3/4 and Nanog in the head and neck squamous carcinoma cells and its clinical implications for delayed neck metastasis in stage I/II oral tongue squamous cell carcinoma. *BMC Cancer* **2015**, *15*, 730.

(53) Fu, T. Y.; Hsieh, I. C.; Cheng, J. T.; Tsai, M. H.; Hou, Y. Y.; Lee, J. H.; Liou, H. H.; Huang, S. F.; Chen, H. C.; Yen, L. M.; et al.etal Association of OCT4, SOX2, and NANOG expression with oral squamous cell carcinoma progression. *J. Oral Pathol.* **2016**, *45* (2), 89−95.

(54) Plaks, V.; Kong, N.; Werb, Z. The cancer stem cell niche: How essential is the niche in regulating stemness of tumor cells. *Cell Stem Cell* **2015**, *16* (3), 225−238.

(55) Siclari, V. A.; Qin, L. Targeting the osteosarcoma cancer stem cell. *J. Orthop. Surg. Res.* **2010**, *5*, 78.

(56) Kundu, B.; Bastos, A. R. F.; Brancato, V.; Cerqueira, M. T.; Oliveira, J. M.; Correlo, V. M.; Reis, R. L.; Kundu, S. C. Mechanical Property of Hydrogels and the Presence of Adipose Stem Cells in Tumor Stroma Affect Spheroid Formation in the 3D Osteosarcoma Model. *ACS Appl. Mater. Interfaces* **2019**, *11* (16), 14548−14559.

(57) Molina, E. R.; Chim, L. K.; Salazar, M. C.; Koons, G. L.; Menegaz, B. A.; Ruiz-Velasco, A.; Lamhamedi-Cherradi, S. E.; Vetter, A. M.; Satish, T.; Cuglievan, B.; et al.et al 3D Tissue-Engineered Tumor Model for Ewing's Sarcoma That Incorporates Bone-like ECM and Mineralization. *ACS Biomater. Sci. Eng.* **2020**, *6* (1), 539−552.

(58) Yazdanpanah, Z.; Johnston, J. D.; Cooper, D. M. L.; Chen, X. 3D Bioprinted Scaffolds for Bone Tissue Engineering: State-Of-The-Art and Emerging Technologies. *Front. Bioeng. Biotechnol.* **2022**, *10*, 824156.

(59) Monteiro, C. F.; Custódio, C. A.; Mano, J. F. *Bioengineering a Humanized 3D Tri-Culture Osteosarcoma Model To Assess Tumor Invasiveness And Therapy Response. Acta Biomater.* **2021**, *134*, 204−214.

(60) Carvalho, M. R.; Lima, D.; Reis, R. L.; Correlo, V. M.; Oliveira, J. M. Evaluating Biomaterial- and Microfluidic-Based 3D Tumor Models. *Trends Biotechnol.* **2015**, *33* (11), 667−678.

(61) Krishnakumar, G. S.; Gostynska, N.; Campodoni, E.; Dapporto, M.; Montesi, M.; Panseri, S.; Tampieri, A.; Kon, E.; Marcacci, M.; Sprio, S.; et al.etal Ribose mediated crosslinking of collagen-hydroxyapatite hybrid scaffolds for bone tissue regeneration using biomimetic strategies. *Mater. Sci. Eng., C* **2017**, *77*, 594−605.

(62) Campodoni, E.; Montanari, M.; Artusi, C.; Bassi, G.; Furlani, F.; Montesi, M.; Panseri, S.; Sandri, M.; Tampieri, A. A Smart

Approach for the Design of Novel Multifunctional Hybrid Materials. *Calcium-Based Biominer.* **2021**, *5* (10), 278.

(63) Mulazzi, M.; Campodoni, E.; Bassi, G.; Montesi, M.; Panseri, S.; Bonvicini, F.; Gentilomi, G. A.; Tampieri, A.; Sandri, M. Medicated Hydroxyapatite/Collagen Hybrid Scaffolds for Bone Regeneration and Local Antimicrobial Therapy to Prevent Bone Infections. *Pharmaceutics* **2021**, *13* (7), 1090.

(64) Ji, J.; Wei, X.; Wang, Y. Embryonic stem cell markers Sox-2 and OCT4 expression and their correlation with WNT signal pathway in cervical squamous cell carcinoma. *Int. J. Clin. Exp. Pathol.* **2014**, *7* (5), 2470−2476.

(65) Zhang, F.; Duan, S.; Tsai, Y.; Keng, P. C.; Chen, Y.; Lee, S. O.; Chen, Y. Cisplatin treatment increases stemness through upregulation of hypoxia-inducible factors by interleukin-6 in non-small cell lung cancer. *Cancer Sci.* **2016**, *107* (6), 746−754.

(66) Lin, J.; Wang, X.; Wang, X.; Wang, S.; Shen, R.; Yang, Y.; Xu, J.; Lin, J. Hypoxia increases the expression of stem cell markers in human osteosarcoma cells. *Oncol. Lett.* **2021**, *21* (3), 217.

(67) Xu, Q. H.; Xiao, Y.; Li, X. Q.; Fan, L.; Zhou, C. C.; Cheng, L.; Jiang, Z. D.; Wang, G. H. Resveratrol Counteracts Hypoxia-Induced Gastric Cancer Invasion and EMT through Hedgehog Pathway Suppression. *Anti-Cancer Agents Med. Chem.* **2020**, *20* (9), 1105−1114.

(68) Ajduković, J. HIF-1–a big chapter in the cancer tale. *Exp. Oncol.* **2016**, *38* (1), 9−12.

(69) Zhang, Q.; Han, Z.; Zhu, Y.; Chen, J.; Li, W. Role of hypoxia inducible factor-1 in cancer stem cells (Review. *Mol. Med. Rep.* **2020**, *23* (1), 17.

(70) Lin, C.; Liao, W.; Jian, Y.; Peng, Y.; Zhang, X.; Ye, L.; Cui, Y.; Wang, B.; Wu, X.; Xiong, Z.; et al.et al CGI-99 promotes breast cancer metastasis via autocrine interleukin-6 signaling. *Oncogene* **2017**, *36* (26), 3695−3705.

(71) Ribatti, D. The chick embryo chorioallantoic membrane (CAM). A multifaceted experimental model. *Mech. Dev.* **2016**, *141*, 70−77.

(72) Kunz, P.; Schenker, A.; Sähr, H.; Lehner, B.; Fellenberg, J. Optimization of the chicken chorioallantoic membrane assay as reliable in vivo model for the analysis of osteosarcoma. *PloS One* **2019**, *14* (4), No. e0215312.

(73) Rauwolf, M.; Pemmer, B.; Roschger, A.; Turyanskaya, A.; Smolek, S.; Maderitsch, A.; Hischenhuber, P.; Foelser, M.; Simon, R.; Lang, S.; et al.et al Increased zinc accumulation in mineralized osteosarcoma tissue measured by confocal synchrotron radiation micro X-ray fluorescence analysis. *X-Ray Spectrom.* **2017**, *46* (1), 56−62.

(74) Li, J.; Zhong, X.-Y.; Li, Z. Y.; Cai, J. F.; Zou, L.; Li, J. M.; Yang, T.; Liu, W. CD133 expression in osteosarcoma and derivation of CD133+ cells. *Mol. Med. Rep.* **2013**, *7* (2), 577−584.

(75) Li, L. T.; Jiang, G.; Chen, Q.; Zheng, J. N. Ki67 is a promising molecular target in the diagnosis of cancer (review. *Mol. Med. Rep.* **2015**, *11* (3), 1566−1572.

(76) Folkman, J. Angiogenesis: An organizing principle for drug discovery? Nature reviews. *Drug Discovery* **2007**, *6* (4), 273−286.

(77) Furuya, M.; Nishiyama, M.; Kasuya, Y.; Kimura, S.; Ishikura, H. Pathophysiology of tumor neovascularization. *Vasc. Health Risk Manage.* **2005**, *1* (4), 277−290.

(78) Newman, P. J.; Newman, D. K. Signal transduction pathways mediated by PECAM-1: New roles for an old molecule in platelet and vascular cell biology. *Arterioscler., Thromb., Vasc. Biol.* **2003**, *23* (6), 953−964.

(79) Tao, Q.; Qi, Y.; Gu, J.; Yu, D.; Lu, Y.; Liu, J.; Liang, X. Breast cancer cells-derived Von Willebrand Factor promotes VEGF-A-related angiogenesis through PI3K/Akt-miR-205−5p signaling pathway. *Toxicol. Appl. Pharmacol.* **2022**, *440*, 115927.

(80) Patmore, S.; Dhami, S. P. S.; O'Sullivan, J. M. Von Willebrand factor and cancer; metastasis and coagulopathies. *J. Thromb. Haemostasis* **2020**, *18* (10), 2444−2456.